

Received May, 2025; revised June, 2025.

# Frequency-Diverse Imaging and Sensing: Electromagnetic-Information Principle, Dispersion Engineering, and Applications

**Qingfeng Zhang, Senior Member, IEEE**  
*(Invited Paper)*

<sup>1</sup>Department of Electronic and Electrical Engineering, Southern University of Science and Technology, Shenzhen, 518055, China

Corresponding author: Q. Zhang (email: zhangqf@sustech.edu.cn).

This work is supported by National Key R&D Program of China (2022YFB2803500) and High-Level Special Funds of SUSTech (G03034K004).

## I. Introduction

Microwave imaging and sensing have emerged as a class of effective non-destructive technologies with diverse applications across medical diagnostics [1]–[6], security screening [7], [8], industrial inspection [9], [10], automotive radar [11], [12], environmental monitoring [13], and integrated sensing and communication (ISAC) [14]–[17]. In healthcare, microwave imaging offers a safe alternative to X-ray imaging for breast cancer detection [1], [2] and brain stroke monitoring [3], [4], leveraging its ability to differentiate tissue dielectric properties. Beyond imaging, microwaves enable non-contact vital-sign monitoring [5], [6], including respiration rate tracking, heartbeat detection, and even fall detection for elderly care, providing continuous, unobtrusive monitoring without wearable sensors. Security systems utilize millimeter-wave and terahertz imaging for concealed object detection [7], [8], while industrial applications include defect detection in materials and structural health assessment [9], [10]. Automotive radar systems, critical for advanced driver-assistance systems (ADAS) and autonomous vehicles, employ microwave sensing to detect objects, measure velocities, and enable adaptive cruise control, enhancing safety through real-time environmental awareness [11], [12]. Additionally, remote sensing with microwaves enables soil moisture measurement, vegetation analysis, and disaster monitoring [13]. In the context of ISAC, microwave systems are increasingly being designed to simultaneously perform wireless communication and sensing tasks [14]–[17], enabling applications such as vehicular radar-communication coexistence, indoor localization, and intelligent infrastructure monitoring. Microwaves' non-ionizing nature, cost-effectiveness, and penetration capabili-

**TABLE 1. Comparison of Various Data Acquisition Techniques in Microwave Imaging and Sensing**

Techniques	Low-Cost	High-Speed	Low-Loss	Simple
MIMO	✗	✓	✓	✓
Mechanical	✓	✗	✓	✓
Switch	✓	✓	✗	✗
Phased Array	✗	✓	✗	✗
Frequency Diverse	✓	✓	✓	✓

ties make them versatile for scientific research and real-world applications.

The core of microwave imaging and sensing lies in the hardware used for data acquisition. Five main techniques are available, as in Tab. 1, each offering distinct trade-offs between cost, speed, loss, and complexity. Multiple-input multiple-output (MIMO) systems, which employ arrays of transmitters and receivers, achieve high spatial resolution by exploiting spatial diversity [18]–[20]. However, the requirement for numerous synchronized transceivers significantly escalates hardware costs and system complexity, driving interest in single-transceiver configurations that balance performance with affordability. Mechanical scanning systems, which physically reposition antennas or sensors, offer simplicity and low electronic complexity but suffer from inherently slow acquisition speeds due to mechanical inertia [21]–[23]. This makes them impractical for real-time applications involving fast-moving targets, such as live physiological monitoring or dynamic security screening.

Reconfigurable antennas based on electronic switches address the speed limitations of mechanical systems by electronically routing signals between radiators [24]–[26]. Still, they introduce insertion losses, particularly at millimeter-wave and terahertz frequencies. The signal degradation from switches and impedance mismatches becomes prohibitive. The biasing network also makes these reconfigurable antennas complicated. Phased arrays, capable of rapid beam steering via analog phase shifters, circumvent mechanical delays but face challenges at high frequencies [27]. Analog phase shifters exhibit significant insertion loss and phase errors, while the extensive usage of active components inflates costs, limiting their use to high-budget applications like defense or astronomy [28].

In contrast, frequency-diverse imaging and sensing exploit frequency-dependent beam patterns [17], [29]–[36], where varying the operating frequency inherently steers the beam without mechanical movement or phase shifters. By leveraging metamaterial structures [29]–[32] or leaky-wave antennas [17], [34]–[36] with frequency-sensitive radiation patterns, this approach enables rapid electronic scanning at minimal hardware cost. The absence of switches and complex phase-shifting networks reduces losses and power consumption, making frequency-diverse systems particularly suited for portable, economic, and real-time imaging and sensing applications.

Frequency-diverse imaging and sensing systems typically employ two primary dispersion engineering approaches to generate frequency-dependent beam patterns. The first approach involves tailoring a radiator's field magnitude to exhibit frequency-dependent characteristics. In this method, the radiating aperture's field magnitude demonstrates sensitive variation with frequency shifts. One may distinguish this dispersion type as *magnitude dispersion*. Prominent implementations of magnitude dispersion include metamaterial radiators [29], [30], Mills-Cross structures [37], and cavity-backed slots [33]. Random distribution techniques are often integrated with metamaterial radiators to mitigate field correlation across frequencies. However, as evidenced in [37], complex metamaterial radiators' imaging performance is inferior to that of the simpler Mills-Cross configuration. It turns out that magnitude dispersion provides no clear structural guidelines for optimal radiator design. Consequently, designers must use computationally intensive optimization techniques to achieve the desired sensing performance. Furthermore, these magnitude dispersion engineered structures typically require huge frequency bandwidths or need to integrate reconfigurable components to achieve good sensing performance [38]–[41].

In contrast to magnitude dispersion, the alternative approach involves engineering frequency-dependent phase variations while maintaining constant field magnitude. One may distinguish this dispersion type as *phase dispersion*. This approach generates high-gain frequency-scanning beams through controlled phase manipulation. The most common

implementations include leaky-wave antennas [42]–[51] and frequency-scanning arrays [52]–[55]. Phase dispersion offers distinct advantages through quantifiable design metrics directly linked to conventional antenna parameters, including beamwidth, gain, angular range, and scanning rate [42]–[44]. Within the framework of phase dispersion engineering, high-scanning-rate leaky-wave antennas [42]–[45], [51] were proposed to reduce the required bandwidth for beam scanning, which not only saves the spectrum resource but also reduces the sampling rate requirement for analog-digital-converter (ADC) in baseband systems. Recent breakthroughs in extremely-high-scanning-rate antennas [53]–[55] have achieved beam scanning using 1% frequency bandwidth only, enabling seamless integration with wireless communication systems for integrated sensing and communication (ISAC) [16], [17], [56]. These advances in phase dispersion engineering have catalyzed numerous novel applications.

This paper presents a systematic treatment of frequency-diverse imaging and sensing, beginning with fundamental principles and progressing to cutting-edge developments in dispersion engineering for antenna design and various novel applications. Sec. II firstly establishes the theoretical foundation through both electromagnetic and information-theoretic perspectives. The analogy with MIMO communication may provide valuable insights into frequency-diverse imaging and sensing. Sec. III subsequently reviews advanced dispersion engineering techniques for frequency-diverse antennas. While magnitude dispersion techniques using metamaterial antennas are well reviewed in [38], this paper focuses on the more recent phase dispersion implementations using leaky-wave antennas and frequency-scanning arrays. Sec. IV further reviews some recent applications and Sec. V finally gives the conclusion.

## II. Principle: Electromagnetic Perspective

### A. Problem Formulation in Spatial Domain

Let us consider the microwave imaging and sensing scenario in Fig. 1. We have a transmitting antenna occupying the space  $V_T$ , a receiving antenna occupying the space  $V_R$ , and a dielectric scatterer occupying the space  $V_S$ . The relative dielectric constant of the scatterer is  $\epsilon_r(\mathbf{r})$  where  $\mathbf{r}$  is the spatial coordinate. As a unit current is excited at the port of the transmitting antenna, a current density  $\mathbf{J}_T$  is generated within space  $V_T$ . Similarly, as a unit current is excited at the port of the receiving antenna, a current density  $\mathbf{J}_R$  is generated within space  $V_R$ . As the electromagnetic wave excited by  $\mathbf{J}_T$  enters the scatterer, it induces a polarization current density  $\mathbf{J}_S$  within space  $V_S$ . The objective of microwave imaging is to reconstruct the geometry of the scatterer, or equivalently, the permittivity distribution  $\epsilon_r(\mathbf{r})$  within  $V_S$ .

As the transmitter is excited, the incident electric field entering the scatterer,  $\mathbf{E}^{ST}$ , is computed by

$$\mathbf{E}^{ST}(\mathbf{r}) = i\omega\mu_0 \int_{V_T} \bar{\mathbf{G}}(\mathbf{r}, \mathbf{r}') \cdot \mathbf{J}_T(\mathbf{r}') d\mathbf{r}', \quad (1)$$

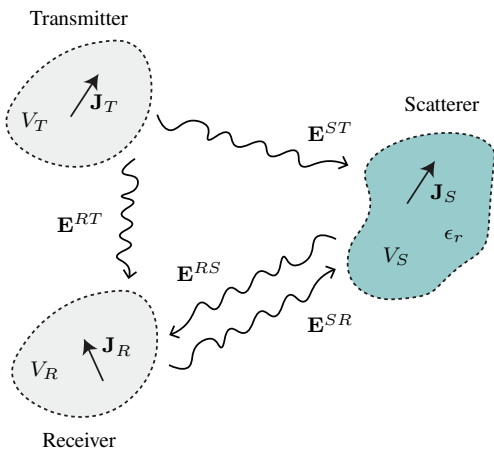


**FIGURE 1.** Scenario of microwave imaging and sensing.

where  $\omega$  is angular frequency,  $\mu_0$  is permeability in free space, and  $\bar{\mathbf{G}}(\mathbf{r}, \mathbf{r}')$  is the dyadic Green's function in free space. The polarization current density induced within the scatterer is

$$\mathbf{J}_S = i\omega\epsilon_0\Delta\epsilon(\mathbf{r})(\mathbf{E}^{ST} + \mathbf{E}^S), \text{ in } V_S, \quad (2)$$

where  $\mathbf{E}^S$  is the scattered electric field,  $\mathbf{E}^{ST} + \mathbf{E}^S$  is the total field,  $\epsilon_0$  is the permittivity in free space, and  $\Delta\epsilon(\mathbf{r}) = \epsilon_r(\mathbf{r}) - 1$  is the contrast of relative permittivity. Under Born approximation, the total field,  $\mathbf{E}^{ST} + \mathbf{E}^S$ , is approximated by the incident field  $\mathbf{E}^{ST}$ . So the polarization current density of (2) is approximated by

$$\mathbf{J}_S \approx i\omega\epsilon_0\Delta\epsilon(\mathbf{r})\mathbf{E}^{ST}. \quad (3)$$

Here, the Born approximation is employed for illustration simplicity. Although various other approximation methods [35], [57] are available for better resolution, the discussion of these algorithm details is beyond the focus of this paper.

The polarization current  $\mathbf{J}_S$  within the scatterer further radiates electric field,  $\mathbf{E}^{RS}$ , to the receiver, which is computed by

$$\mathbf{E}^{RS}(\mathbf{r}) = i\omega\mu_0 \int_{V_S} \bar{\mathbf{G}}(\mathbf{r}, \mathbf{r}') \cdot \mathbf{J}_S(\mathbf{r}') d\mathbf{r}'. \quad (4)$$

The total field entering the receiver,  $\mathbf{E}_\text{total}^R$ , has two parts, i.e.  $\mathbf{E}_\text{total}^R = \mathbf{E}^{RS} + \mathbf{E}^{RT}$ , where  $\mathbf{E}^{RT}$  is the direct radiation from the transmitter and  $\mathbf{E}^{RS}$  is the indirect radiation due to the scatterer.

According to the classic reaction theorem proposed by V. H. Rumsey [58] and R. F. Harrington [59], the voltage induced at the port of the receiving antenna,  $v_R$ , is calculated through the reaction, i.e.

$$v_R = \langle \mathbf{J}_R, \mathbf{E}_\text{total}^R \rangle = \langle \mathbf{J}_R, \mathbf{E}^{RT} \rangle + \langle \mathbf{J}_R, \mathbf{E}^{RS} \rangle, \quad (5)$$

where the inner product  $\langle \mathbf{J}, \mathbf{E} \rangle = \int_{V_J} \mathbf{J} \cdot \mathbf{E} d\mathbf{r}$  defines the reaction between the source  $\mathbf{J}$  in  $V_J$  and outer space. One should note that unit currents are used in both the transmitter and receiver ports in calculating  $v_R$  in (5). Otherwise, this quantity should be normalized with respect to the excitation

currents at the ports. Note from (5) that the induced voltage at the receiving port is contributed by two parts, where  $\langle \mathbf{J}_R, \mathbf{E}^{RT} \rangle$  is the background reaction without the scatterer and  $\langle \mathbf{J}_R, \mathbf{E}^{RS} \rangle$  is the additional reaction contributed by the scatterer. One may calibrate out this background reaction by removing the receiving voltage without the scatterer, which is denoted as  $v_{R0} = \langle \mathbf{J}_R, \mathbf{E}^{RT} \rangle$ . So one defines a voltage variation  $\Delta v_R = v_R - v_{R0}$ , which, upon substitution of (5), reads

$$\Delta v_R = \langle \mathbf{J}_R, \mathbf{E}^{RS} \rangle. \quad (6)$$

According to reciprocity theorem, one has  $\langle \mathbf{J}_R, \mathbf{E}^{RS} \rangle = \langle \mathbf{J}_S, \mathbf{E}^{SR} \rangle$ , where  $\mathbf{E}^{SR}$ , being the electric field within the scatterer due to the radiation of  $\mathbf{J}_R$ , can be computed by

$$\mathbf{E}^{SR}(\mathbf{r}) = i\omega\mu_0 \int_{V_R} \bar{\mathbf{G}}(\mathbf{r}, \mathbf{r}') \cdot \mathbf{J}_S(\mathbf{r}') d\mathbf{r}'. \quad (7)$$

Therefore, the voltage variation in (6) is reformulated as

$$\Delta v_R = \langle \mathbf{J}_S, \mathbf{E}^{SR} \rangle, \quad (8)$$

which, upon substitution of (3), becomes

$$\begin{aligned} \Delta v_R &= i\omega\epsilon_0 \langle \Delta\epsilon(\mathbf{r})\mathbf{E}^{ST}, \mathbf{E}^{SR} \rangle \\ &= i\omega\epsilon_0 \int_{V_S} \Delta\epsilon(\mathbf{r})\mathbf{E}^{ST}(\mathbf{r}) \cdot \mathbf{E}^{SR}(\mathbf{r}) d\mathbf{r}. \end{aligned} \quad (9)$$

Note from (9) that the voltage variation received at the port is proportional to a weighted average of permittivity contrast  $\Delta\epsilon(\mathbf{r})$  within the scatterer and the weighting coefficient,  $\mathbf{E}^{ST}(\mathbf{r}) \cdot \mathbf{E}^{SR}(\mathbf{r})$ , is determined by the designed transmitter and receiver according to (1) and (7). However, the single equation (9) is not enough to recover the unknown  $\Delta\epsilon(\mathbf{r})$ . More equations are demanded by changing the weighting coefficient  $\mathbf{E}^{ST}(\mathbf{r}) \cdot \mathbf{E}^{SR}(\mathbf{r})$ .

The essence of frequency-diverse imaging is to produce a highly dispersive  $\mathbf{E}^{ST}$ , or  $\mathbf{E}^{SR}$ , or both, while assuming the scatterer permittivity is non-dispersive or very weakly dispersive within an operational bandwidth. In this case, one can test (9) at various frequencies to achieve many equations for the recovery of unknown  $\Delta\epsilon(\mathbf{r})$ . The frequency-dependent version of (9) is

$$\Delta v_R(\omega) = i\epsilon_0 \int_{V_S} \Delta\epsilon(\mathbf{r})\omega\mathbf{E}^{ST}(\mathbf{r}, \omega) \cdot \mathbf{E}^{SR}(\mathbf{r}, \omega) d\mathbf{r}. \quad (10)$$

One subsequently discretizes the volumetric space  $V_S$  into  $N$  samples with each one occupying  $\Delta V$  and their center positions form a vector  $[\mathbf{r}_1, \mathbf{r}_2, \dots, \mathbf{r}_N]$ . One also discretizes the operational frequency band into  $M$  samples, i.e.  $[\omega_1, \omega_2, \dots, \omega_M]$ . Then the equations of (10) at various frequencies are expressed using matrix formulation, i.e.

$$\mathbf{H}\boldsymbol{\varepsilon} = \boldsymbol{\nu}, \quad (11)$$

where  $\boldsymbol{\nu} = [\Delta v_R(\omega_1), \Delta v_R(\omega_2), \dots, \Delta v_R(\omega_M)]^T$ ,  $\boldsymbol{\varepsilon} = [\Delta\epsilon(\mathbf{r}_1), \Delta\epsilon(\mathbf{r}_2), \dots, \Delta\epsilon(\mathbf{r}_N)]^T$ , and  $\mathbf{H}$  is an  $M \times N$  matrix whose entry at  $m^{\text{th}}$  row and  $n^{\text{th}}$  column reads

$$H_{mn} = i\epsilon_0\omega_m \mathbf{E}^{ST}(\mathbf{r}_n, \omega_m) \cdot \mathbf{E}^{SR}(\mathbf{r}_n, \omega_m) \Delta V. \quad (12)$$

In frequency-diverse imaging, the key is to solve the linear equation (11), where  $\varepsilon$  has the unknown permittivity to be recovered,  $\nu$  gives the measured voltages at the receiving port, and  $\mathbf{H}$  is called the measurement matrix which contains all the information about the transmitting and receiving antennas. To well recover  $\varepsilon$ , the  $M$  rows in  $\mathbf{H}$  should be as independent as possible. Equivalently, according to (12), the electric field product,  $\mathbf{E}^{ST} \cdot \mathbf{E}^{SR}$ , within the imaging region should be as dispersive as possible so that this quantity changes significantly with frequency. According to (1) and (7), the electric field within the imaging domain is determined by the excited current density in the transmitter and receiver. Therefore, the key to frequency-diverse imaging and sensing is to tailor the dispersive current densities of the transmitting and receiving antennas. How to mathematically evaluate the imaging performance of a tailored antenna will be introduced in Sec. III.

### B. Formulation in Spectral Domain

As introduced in (11) and (12), the imaging and sensing performance is mainly determined by the product of the transmitting field and the receiving field within the imaging domain, which are further affected by the current distribution on the transmitting and receiving apertures. This part will employ spectral-domain analysis to relate the radiated field and the aperture current, which may provide better insights into the design of antennas for frequency-diverse microwave imaging and sensing.

According to (1), the radiated field  $\mathbf{E}^{ST}(\mathbf{r})$  is linked to the antenna current  $\mathbf{J}_T(\mathbf{r})$  by a dyadic Green's function which is expressed by [60]

$$\tilde{\mathbf{G}}(\mathbf{r}, \mathbf{r}') = \left( \bar{\mathbf{I}} + \frac{\nabla \nabla}{k_0^2} \right) \frac{e^{-ik_0|\mathbf{r}-\mathbf{r}'|}}{4\pi|\mathbf{r}-\mathbf{r}'|}, \quad (13)$$

where  $\bar{\mathbf{I}}$  is the unit dyadic,  $k_0 = \omega\sqrt{\epsilon_0\mu_0}$  is wavenumber in free space. Let us express  $\mathbf{J}_T(\mathbf{r})$  and  $\mathbf{E}^{ST}(\mathbf{r})$  in (1) using plane-wave decomposition in spectral domain, i.e.

$$\mathbf{J}_T(\mathbf{r}) = \frac{1}{(2\pi)^3} \int \tilde{\mathbf{J}}_T(\mathbf{k}) e^{-j\mathbf{k}\cdot\mathbf{r}} d\mathbf{k}, \quad (14)$$

$$\mathbf{E}^{ST}(\mathbf{r}) = \frac{1}{(2\pi)^3} \int \tilde{\mathbf{E}}^{ST}(\mathbf{k}) e^{-j\mathbf{k}\cdot\mathbf{r}} d\mathbf{k}. \quad (15)$$

By substituting (14) and (15) into (1) and applying the Fourier transformation of the dyadic Green's function in (13), one obtains [60]

$$\tilde{\mathbf{E}}^{ST}(\mathbf{k}) = \frac{i\omega\mu_0}{k^2 - k_0^2} \left( \bar{\mathbf{I}} - \frac{\mathbf{k}\mathbf{k}}{k_0^2} \right) \cdot \tilde{\mathbf{J}}_T(\mathbf{k}) \quad (16)$$

$$= \frac{i\omega\mu_0}{k^2 - k_0^2} \left( \bar{\mathbf{I}} - \hat{\mathbf{k}}\hat{\mathbf{k}} \right) \cdot \tilde{\mathbf{J}}_T(\mathbf{k}) + \frac{\hat{\mathbf{k}}\hat{\mathbf{k}}}{i\omega\epsilon_0} \cdot \tilde{\mathbf{J}}_T(\mathbf{k}) \quad (17)$$

$$= \frac{i\omega\mu_0}{k^2 - k_0^2} \tilde{\mathbf{J}}_T^\perp(\mathbf{k}) + \frac{1}{i\omega\epsilon_0} \tilde{\mathbf{J}}_T^\parallel(\mathbf{k}), \quad (18)$$

where  $\tilde{\mathbf{J}}_T^\parallel = \hat{\mathbf{k}}\hat{\mathbf{k}} \cdot \tilde{\mathbf{J}}_T$  denotes the longitudinal part of  $\tilde{\mathbf{J}}_T$ , and  $\tilde{\mathbf{J}}_T^\perp = (\bar{\mathbf{I}} - \hat{\mathbf{k}}\hat{\mathbf{k}}) \cdot \tilde{\mathbf{J}}_T$  denotes the transverse part of

$\tilde{\mathbf{J}}_T$ . The physical meaning of (18) is straightforward, i.e., the electric field is contributed by both longitudinal and transverse parts of the current density. The longitudinal part denotes the contribution from charges due to the continuity equation, which only dominates in the near-field region. As the distance increases, the transverse part plays a major role in the radiated field. So the electric field can be approximated by the transverse contribution of the electric current.

Similarly, one also relates the electric field to the current density on the receiver in the spectral domain by

$$\tilde{\mathbf{E}}^{SR}(\mathbf{k}) = \frac{i\omega\mu_0}{k^2 - k_0^2} \tilde{\mathbf{J}}_R^\perp(\mathbf{k}) + \frac{1}{i\omega\epsilon_0} \tilde{\mathbf{J}}_R^\parallel(\mathbf{k}), \quad (19)$$

where  $\tilde{\mathbf{E}}^{SR}$  denotes the spectral-domain electric field excited by the spectral-domain transverse  $\tilde{\mathbf{J}}_R^\perp$  and longitudinal  $\tilde{\mathbf{J}}_R^\parallel$  currents on the receiver.

According to (12), the element of the measurement matrix is proportional to the multiplication of  $\mathbf{E}^{ST}(\mathbf{r})$  and  $\mathbf{E}^{ST}(\mathbf{r})$  in the spatial domain. Let's define the product of the two fields as  $h(\mathbf{r}) = \mathbf{E}^{ST}(\mathbf{r}) \cdot \mathbf{E}^{ST}(\mathbf{r})$ , and its spectral-domain representation is  $\tilde{h}(\mathbf{k})$ . According to the characteristics of the Fourier transformation, the multiplication in the spatial domain is equivalent to the convolution in the spectral domain. So one has

$$\tilde{h}(\mathbf{k}) = \frac{1}{(2\pi)^3} \int \tilde{\mathbf{E}}^{ST}(\mathbf{k}') \cdot \tilde{\mathbf{E}}^{SR}(\mathbf{k} - \mathbf{k}') d\mathbf{k}', \quad (20)$$

which, upon substitution of (18) and (19) by considering the transverse currents only, becomes

$$\tilde{h}(\mathbf{k}) \approx \frac{-\omega^2\mu_0^2}{(2\pi)^3} \int \frac{\tilde{\mathbf{J}}_T^\perp(\mathbf{k}') \cdot \tilde{\mathbf{J}}_R^\perp(\mathbf{k} - \mathbf{k}')}{(k'^2 - k_0^2)[(k - k')^2 - k_0^2]} d\mathbf{k}'. \quad (21)$$

In frequency-diverse microwave imaging and sensing, it requires that  $h(\mathbf{r})$ , or equivalently  $\tilde{h}(\mathbf{k})$ , changes sensitively with frequency. According to (21), it is equivalent to say that the convolution of  $\tilde{\mathbf{J}}_T^\perp$  and  $\tilde{\mathbf{J}}_R^\perp$  should be as dispersive as possible. Suppose one employs a leaky-wave antenna as the transmitter or receiver. In that case, it will produce a pulse-shape angular radiation spectrum,  $\tilde{\mathbf{J}}^\perp(\hat{\mathbf{k}})$ , which has a peak at a specific direction controlled by frequency. As the operating frequency varies, the principal radiation direction shifts accordingly, thereby inducing corresponding modifications of  $\tilde{\mathbf{J}}^\perp(\hat{\mathbf{k}})$  and  $\tilde{h}(\mathbf{k})$ . The angular spectrum convolution of  $\tilde{\mathbf{J}}_T^\perp$  and  $\tilde{\mathbf{J}}_R^\perp$  will probe the spectrum of the imaging region. This explains the operational principle of leaky-wave antennas for frequency-diverse microwave imaging and sensing.

### III. Principle: Information-Theoretic Perspective

The above section has introduced the principle of frequency-diverse microwave imaging and sensing. The spatial-domain analysis of Sec. II-A shows that the fields radiated by the transmitter and receiver within the imaging region should be as dispersive as possible to provide more independent equations to solve (11). The product of the fields by the transmitter and receiver determines the measurement matrix. The spectral-domain analysis of Sec. II-B indicates that the

radiation spectrum of the transmitter and receiver should be as dispersive as possible. The spectrum convolution of the transmitter and receiver probes the spectrum of the imaging region. However, these only provide a qualitative evaluation for the design of transmitting and receiving antennas in frequency-diverse microwave imaging. They cannot provide a thorough quantitative evaluation. For instance, in the case of leaky-wave antennas for frequency-diverse microwave imaging, Sec. II-B only tells that the radiation beam should sensitively change with frequency. But how is the effect of other parameters, e.g. beamwidth, angular range, efficiency, and many others. All of these cannot be easily evaluated. This section will provide an information-theoretic metrics for the design of antennas in frequency-diverse microwave imaging and sensing.

#### A. Singular Value Decomposition of Measurement Matrix

The key to frequency-diverse microwave imaging and sensing is to solve the linear problem in (11), where the measurement matrix  $\mathbf{H}$  connects unknowns with the measured voltages. If each row of  $\mathbf{H}$  is less correlated with each other, it provides more independent equations to solve the unknowns, and it is equivalent to saying that it has a better sensing capacity. A mathematical tool to quantitatively analyze this is through singular value decomposition (SVD) of  $\mathbf{H}$  [34], [61]. One decomposes the  $M \times N$  measurement matrix ( $M \leq N$ ),  $\mathbf{H}$ , into three sub matrices [62],

$$\mathbf{H} = \mathbf{U}\Sigma\mathbf{V}^\dagger, \quad (22)$$

where  $\dagger$  denotes the conjugate transpose of a complex matrix.  $\mathbf{U}$  is called left singular matrix which is an  $M \times M$  unitary matrix satisfying  $\mathbf{U}\mathbf{U}^\dagger = \mathbf{U}^\dagger\mathbf{U} = \mathbf{I}$  where  $\mathbf{I}$  is an identity matrix.  $\Sigma$  is an  $M \times N$  matrix whose entries are zeros except the diagonal entries storing  $M$  decreasing non-negative real singular values  $\{\sigma_1, \sigma_2, \dots, \sigma_M\}$ .  $\mathbf{V}$  is called right singular matrix which is an  $N \times N$  unitary matrix satisfying  $\mathbf{V}\mathbf{V}^\dagger = \mathbf{V}^\dagger\mathbf{V} = \mathbf{I}$ . The column vectors of  $\mathbf{U}$ ,  $\{\mathbf{u}_1, \mathbf{u}_2, \dots, \mathbf{u}_M\}$ , spans an  $M$ -dimensional vector space as orthogonal vectors. The column vectors of  $\mathbf{V}$ ,  $\{\mathbf{v}_1, \mathbf{v}_2, \dots, \mathbf{v}_N\}$ , spans an  $N$ -dimensional vector space as orthogonal vectors.

The SVD has a long and rich history in mathematics and engineering applications. It is widely employed in image compression [63], signal processing [64], wireless communication [65], and control theory [66]. A good review on the early history of SVD can be found in [67]. There are many ways to understand the essential physical meaning of SVD in frequency-diverse imaging. A simple way is through the correlation matrices  $\mathbf{H}\mathbf{H}^\dagger$  and  $\mathbf{H}^\dagger\mathbf{H}$ , where the former calculates the correlation between all the row vectors of  $\mathbf{H}$  and the latter computes the correlation between all the column vectors of  $\mathbf{H}$ . The two correlation matrices tell us how dependent the interaction between electromagnetic waves and objects is in frequency and spatial space, respectively.

By applying (22), one easily obtains

$$\mathbf{H}\mathbf{H}^\dagger = \mathbf{U}\Sigma\mathbf{V}^\dagger\mathbf{V}\Sigma^T\mathbf{U}^\dagger = \mathbf{U}\Sigma\Sigma^T\mathbf{U}^\dagger, \quad (23)$$

$$\mathbf{H}^\dagger\mathbf{H} = \mathbf{V}\Sigma^T\mathbf{U}^\dagger\mathbf{U}\Sigma\mathbf{V}^\dagger = \mathbf{V}\Sigma^T\Sigma\mathbf{V}^\dagger. \quad (24)$$

Note from (23) that  $\Sigma\Sigma^T$  is a diagonal matrix whose diagonal entries,  $\{\sigma_1^2, \sigma_2^2, \dots, \sigma_M^2\}$ , are the eigenvalues of  $\mathbf{H}\mathbf{H}^\dagger$  and the column vectors of  $\mathbf{U}$  are the eigenvectors of  $\mathbf{H}\mathbf{H}^\dagger$ . Similarly, note from (24) that the column vectors of  $\mathbf{V}$  are the eigenvectors of  $\mathbf{H}^\dagger\mathbf{H}$ . One may call the space spanned by  $\{\mathbf{u}_1, \mathbf{u}_2, \dots, \mathbf{u}_M\}$  as frequency space, and the space spanned by  $\{\mathbf{v}_1, \mathbf{v}_2, \dots, \mathbf{v}_N\}$  as spatial space, in frequency-diverse imaging.

The singular values in  $\Sigma$  are good indicators for the number of independent equations that can be used to solve the imaging problem in (11). Since the singular values are arranged in a decreasing order and only nonzero singular values indicate independent equations, the first  $r$  nonzero singular values,  $\{\sigma_1, \sigma_2, \dots, \sigma_r\}$ , denote  $r$  independent equations that can be used to solve (11).  $r$  also corresponds to the rank of  $\mathbf{H}$ . One usually calls these independent equations as independent measurement modes [34], [61]. So one has  $r$  independent measurement modes if  $r$  nonzero singular values exist in  $\Sigma$ . The magnitude of the singular value indicates the significance of the corresponding measurement. Larger magnitudes of singular values indicate higher sensing capability for the designed antennas. In most practical applications, one does not truncate the singular values until zero because too small singular values (for less significant measurements) may be buried in noise. Therefore, one may set a threshold  $\delta$  and count the number of singular values above  $\delta$ . The choice of  $\delta$  depends on the noise level in measurement, and more theoretical discussions on the choice of the threshold can be found in [68].

Another way to understand and use the SVD analysis in frequency-diverse imaging is through the Eckart-Young theorem [69]. It states that, for a required rank  $r$ , the least-square approximation to  $\mathbf{H}$  is through the rank- $r$  SVD truncation, i.e.  $\bar{\mathbf{H}} = \bar{\mathbf{U}}\bar{\Sigma}\bar{\mathbf{V}}^\dagger$ , where  $\bar{\mathbf{U}}$  and  $\bar{\mathbf{V}}$  picks the first  $r$  columns of  $\mathbf{U}$  and  $\mathbf{V}$ , and  $\bar{\Sigma}$  denotes the leading  $r \times r$  submatrix of  $\Sigma$ . The approximated matrix  $\bar{\mathbf{H}}$  can be expressed as matrix expansion [62],

$$\bar{\mathbf{H}} = \sum_{\ell=1}^r \sigma_\ell \mathbf{u}_\ell \mathbf{v}_\ell^\dagger = \sigma_1 \mathbf{u}_1 \mathbf{v}_1^\dagger + \sigma_2 \mathbf{u}_2 \mathbf{v}_2^\dagger + \dots + \sigma_r \mathbf{u}_r \mathbf{v}_r^\dagger, \quad (25)$$

where  $\mathbf{u}_\ell \mathbf{v}_\ell^\dagger$  are  $M \times N$  rank-1 matrices. This approximation is widely used in image compression. In frequency-diverse imaging, such an approximation approach is essential to reduce the measurement size if the measurement matrix is compressible. This is true in most practical frequency-diverse imaging applications [34], [61]. For instance, although we sample the measurement frequency very densely, most frequencies may be redundant and cannot provide independent measurements. This indicates that the high-dimensional measurements may contain low-dimensional patterns. The truncated SVD basis in  $\bar{\mathbf{U}}$  and  $\bar{\mathbf{V}}$  maps the

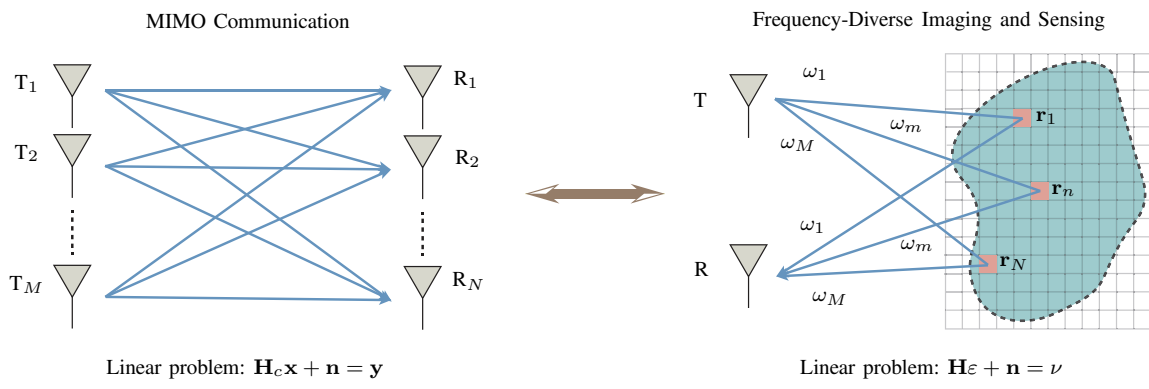


**FIGURE 2.** Analogy between MIMO communication and frequency-diverse imaging and sensing in real space.

high-dimensional measurement space to a low-dimensional pattern space. The compressible feature of the measurement matrix has recently been employed to build and calibrate the measurement matrix for frequency-diverse microwave imaging [70], [71].

The SVD also has other useful properties that can be applied to frequency-diverse imaging and sensing. For instance, the SVD terms are invariant after multiplying a unitary matrix except the corresponding  $\mathbf{U}$  or  $\mathbf{V}$ . This can be applied to the discrete Fourier transform (DFT), which is unitary. In the frequency-diverse imaging problem of (11), one may multiply  $\mathbf{H}$  by a DFT matrix on the right, which transforms the spatial domain to the spectral domain and reformulates the original problem in the frequency-spectral domain. This operation changes  $\mathbf{V}$  only, and meanwhile preserves  $\mathbf{U}$  and  $\Sigma$ . Similarly, one may multiply  $\mathbf{H}$  by a DFT matrix on the left, transforming the frequency domain to the temporal domain and reformulating the original problem in the temporal-spatial domain. This operation changes  $\mathbf{U}$  only, and meanwhile preserves  $\mathbf{V}$  and  $\Sigma$ .

### B. Analogy to MIMO Communication

To better quantify the sensing capacity of frequency-diverse antennas, let us make an analogy between MIMO communication and frequency-diverse imaging and sensing, as shown in Fig. 2. Such an analogy also bridges frequency-diverse imaging and MIMO communication, which may promote the application of frequency-diverse imaging in ISAC.

As shown in the left figure of Fig. 2, MIMO communication employs  $M$  transmitting antennas as input and  $N$  receiving antennas as output. It is modeled as the following linear problem [72]:

$$\mathbf{H}_c \mathbf{x} + \mathbf{n} = \mathbf{y}, \quad (26)$$

where  $\mathbf{H}_c \in \mathbb{C}^{M \times N}$  is the channel matrix,  $\mathbf{x} \in \mathbb{C}^{M \times 1}$  is the transmitted signal vector,  $\mathbf{n} \in \mathbb{C}^{N \times 1}$  is the Gaussian noise vector in the channel, and  $\mathbf{y} \in \mathbb{C}^{N \times 1}$  is the received signal vector. The transmitting system modulates information and then transmits it from  $M$  transmitting antennas to  $N$  receiving antennas. Multiple communication channels exist, characterized by the channel matrix  $\mathbf{H}_c$ .

The frequency-diverse imaging and sensing has a similar mechanism, as shown in the right figure of Fig. 2. Although it only employs one transmitting antenna and one receiving antenna, the frequency-diverse antennas can change beam patterns. Hence, multiple channels exist for the interaction between electromagnetic waves and matter (dielectric scatterer). In the case of leaky-wave antennas, different frequencies result in different beam directions, leading to various interactions with different parts of the scatterer. One employs the measurement matrix  $\mathbf{H}$  to characterize the interaction channels between wave and scatterer. The frequency-diverse imaging and sensing solve the linear problem in (11), which, if considering measurement noise, may be formulated as

$$\mathbf{H}\epsilon + \mathbf{n} = \nu, \quad (27)$$

where  $\mathbf{n} \in \mathbb{C}^{N \times 1}$  is the Gaussian noise vector in the measurement. Note that frequency-diverse imaging and sensing is very similar to MIMO communication. The measurement matrix  $\mathbf{H}$  corresponds to the channel matrix  $\mathbf{H}_c$ , and the interaction channel corresponds to the communication channel. The only difference is that the information is modulated by the scatterer in frequency-diverse imaging and sensing, whereas it is modulated by the transmitting system in MIMO communication. Such an analogy also provides more inspiration if one combines the two for ISAC applications, where information sources exist in both the environmental scatterer and the transmitter.

Based on the analogy between MIMO communication and frequency-diverse imaging in Fig. 2, one may further apply the SVD to both channels. Assume  $\mathbf{H}_c = \mathbf{U}_c \Sigma_c \mathbf{V}_c^\dagger$ , where  $\mathbf{U}_c \in \mathbb{C}^{M \times M}$  is the left singular matrix,  $\Sigma_c \in \mathbb{C}^{M \times N}$  stores all the singular values  $\{\sigma_1^c, \sigma_2^c, \dots, \sigma_M^c\}$  in its diagonal entries, and  $\mathbf{V}_c \in \mathbb{C}^{N \times N}$  is the right singular matrix. By substituting  $\mathbf{H}_c = \mathbf{U}_c \Sigma_c \mathbf{V}_c^\dagger$  to (26) and left multiplying  $\mathbf{U}_c^\dagger$  on both sides of the equation, one has

$$\Sigma_c \mathbf{V}_c^\dagger \mathbf{x} + \mathbf{U}_c^\dagger \mathbf{n} = \mathbf{U}_c^\dagger \mathbf{y}, \quad (28)$$

which, by using  $\mathbf{x}' = \mathbf{V}_c^\dagger \mathbf{x}$ ,  $\mathbf{y}' = \mathbf{U}_c^\dagger \mathbf{y}$ , and  $\mathbf{n}' = \mathbf{U}_c^\dagger \mathbf{n}$ , is further simplified as

$$\Sigma_c \mathbf{x}' + \mathbf{n}' = \mathbf{y}'. \quad (29)$$

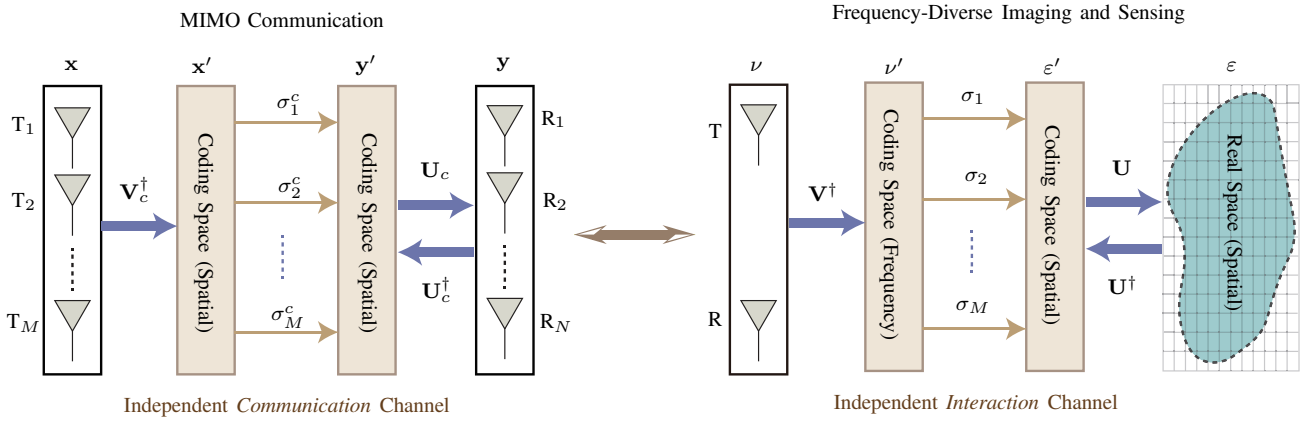


**FIGURE 3.** Analogy between MIMO communication and frequency-diverse imaging and sensing in coding space by applying SVD.

One may call  $x'$  and  $y'$  as signals in coding space, and  $V_c$  and  $U_c$  provide transformations between real space and coding space. Note from (29) that all the communication channels in coding space are independent and  $\{|\sigma_1^c|^2, |\sigma_2^c|^2, \dots, |\sigma_M^c|^2\}$  are channel gains. This has been illustrated in the left figure of Fig. 3.

Similarly, for frequency-diverse imaging and sensing, one also substitutes the SVD in (22) to (27) and left multiplies  $U^\dagger$  on both sides of the equation, leading to

$$\Sigma\epsilon' + n' = \nu' , \quad (30)$$

where  $\epsilon' = V^\dagger\epsilon$ ,  $\nu' = U^\dagger\nu$ , and  $n' = U^\dagger n$ . As shown in the right figure of Fig. 3, we also obtain a coding space  $\epsilon'$  for the imaging object in the spatial domain and a coding space  $\nu'$  for the detected signal in the frequency domain. In the coding space, all the interaction channels are independent, and  $\{|\sigma_1|^2, |\sigma_2|^2, \dots, |\sigma_M|^2\}$  are interaction gains of each channel. Therefore, one has established an exact one-to-one correspondence between MIMO communication and frequency-diverse imaging and sensing.

Based on this correspondence, one may further define an interaction capacity or sensing capacity for frequency-diverse imaging and sensing, as an analogy to the channel capacity in MIMO communication [72]. Such an interaction or sensing capacity, measured in bits, is expressed as [34], [61], [73]

$$C_{\text{int}} = \sum_{\ell=1}^M \log_2 \left( 1 + \frac{P_\ell \sigma_\ell^2}{N_0} \right) , \quad (31)$$

where  $P_\ell/N_0$  denotes SNR of the  $\ell^{\text{th}}$  interaction channel. This interaction capacity can be employed to evaluate the antenna design for frequency-diverse imaging and sensing quantitatively.

### C. Illustrative Examples Using Leaky-Wave Antennas

To better illustrate the information-theoretic metrics proposed in the above section, one may consider a simplified 1-D imaging example on the  $xy$ -plane using a 1-D leaky-wave antenna, as shown in Fig. 4. The transmitter employs a 1-D leaky-wave antenna with  $z$ -polarized current density

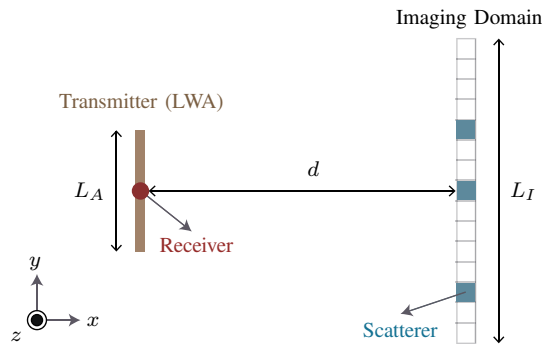


**FIGURE 4.** 1-D imaging example using a 1-D leaky-wave antenna (LWA) as the transmitter and an omnidirectional point source as the receiver.

distributed along  $y$ -axis from  $[0, -L_A/2]$  to  $[0, L_A/2]$ . The receiver employs an omnidirectional point source located at the origin. The imaging domain is a 1-D region distributed from  $[d, -L_I/2]$  to  $[d, L_I/2]$ . The current density of the point-source receiver is expressed as

$$J_R(x, y) = J_{R0} \delta(x) \delta(y) \hat{z} , \quad (32)$$

where  $J_{R0}$  is a normalization constant. The current density of the leaky-wave antenna transmitter is expressed as

$$J_T(x, y) = J_{T0} \delta(x) e^{-i\beta(\omega)y} \hat{z} , \quad (33)$$

where  $y \in [-L_A/2, L_A/2]$ ,  $J_{T0}$  is a normalization constant, and  $\beta$  is propagation constant of the leaky-wave antenna. Assume the leaky-wave antenna scans a radiation beam around broadside ( $x$ -axis) and the corresponding broadside frequency is  $\omega_0$ . Then the propagation constant around the broadside can be written as

$$\beta(\omega) = \frac{2\pi\varrho}{\lambda_0} \left( \frac{\omega}{\omega_0} - 1 \right) , \quad (34)$$

where  $\lambda_0$  is the space wavelength at  $\omega_0$ , and  $\varrho$  is usually called scanning rate [43], [44], which is defined to indicate the sensitivity of the beam angle to varied frequencies.

To better see the physical meaning of the scanning rate  $\varrho$ , let us compute the beam angle with respect to  $x$ -axis,  $\theta$ ,

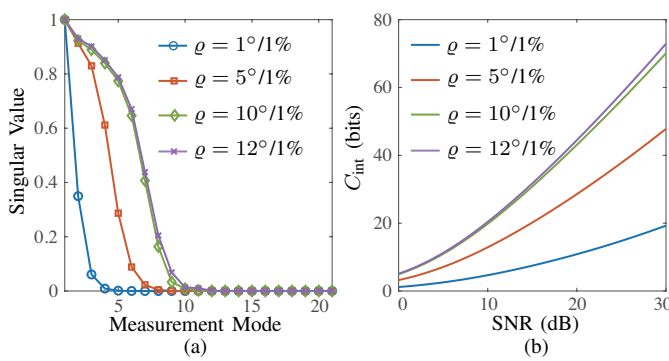


**FIGURE 5.** (a) Singular value distributions and (b) interaction capacities for a 1-D leaky-wave antenna with different scanning rates  $\rho$  while maintaining  $L_I = 8\lambda_0$ .

which satisfies

$$\sin \theta = \frac{\beta(\omega)}{k_0}. \quad (35)$$

Upon substitution of (34), the equation (35) becomes

$$\sin \theta = \varrho \left(1 - \frac{\omega_0}{\omega}\right). \quad (36)$$

As  $\omega = \omega_0$ , one gets  $\theta = 0$ , corresponding to broadside. Within a small angular range around the broadside, one has  $\sin \theta \approx \theta$ . So one easily finds from (36) that

$$\varrho = \frac{d\theta}{d\left(\frac{\omega}{\omega_0}\right)}, \text{ at } \omega = \omega_0. \quad (37)$$

Therefore, the scanning rate indicates the beam angle variation to the relative frequency variation around the broadside.

Let us now consider a specific example, where  $L_A = 4\lambda_0$ ,  $L_I = 8\lambda_0$ ,  $d = 3\lambda_0$ , and  $\Delta\omega/\omega_0 = 10\%$ . Then one may sample the frequency bandwidth into  $M = 21$  points and sample the imaging domain into  $N = 100$  elements. Firstly, let us illustrate the effect of scanning rate on the mode diversity, which is defined by the number of measurement modes with nonzero singular values. Fig. 5 shows the singular value distributions and interaction capacities for different scanning rates  $\varrho$ . Note that mode diversity and interaction capacity increase as the scanning rate increases. This can be understood by considering the angle range the radiation beam scans within  $\Delta\omega/\omega_0 = 10\%$  bandwidth. As the scanning rate varies from  $1^\circ/1\%$  to  $12^\circ/1\%$ , the scanned angle range increases from  $10^\circ$  to approximately  $120^\circ$ . According to (21), a larger scanned angle range, corresponding to a significant variation of  $\tilde{\mathbf{J}}_T^\perp(\mathbf{k})$  at different frequencies, will provide more diversities for  $\tilde{h}(\mathbf{k})$ . This explains why the mode diversity increases with the scanning rate. Also, while increasing the scanning rate from  $10^\circ/1\%$  to  $12^\circ/1\%$ , the mode diversity and interaction capacity exhibit negligible growth. Such a saturation phenomenon is attributed to the limited field of view (FoV) spanned by the imaging domain, which is approximately  $106^\circ$  in this case. As the scanning rate increases to  $10^\circ/1\%$ , the scanned angle range reaches  $100^\circ$ , which is very close to the FoV

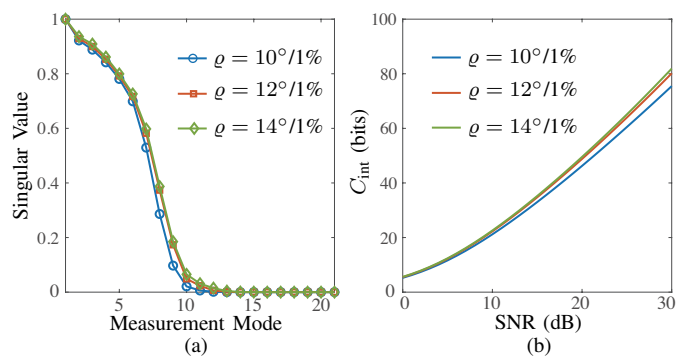


**FIGURE 6.** (a) Singular value distributions and (b) interaction capacities for a 1-D leaky-wave antenna with different scanning rates  $\rho$  while maintaining  $L_I = 12\lambda_0$ .

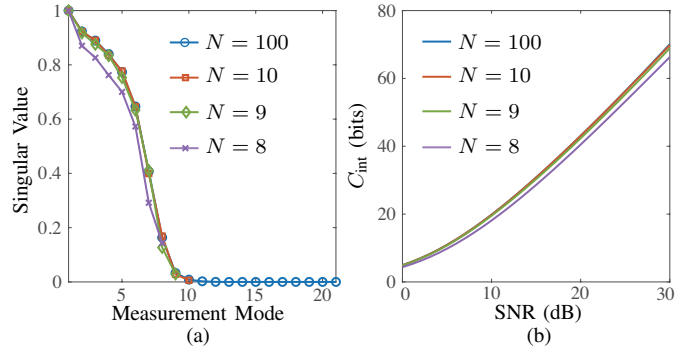


**FIGURE 7.** (a) Singular value distributions and (b) interaction capacities for different sampling number  $N$  in imaging domain, while maintaining  $\rho = 10^\circ/1\%$  and  $L_I = 8\lambda_0$ .

of the imaging domain. If one further increases the scanning rate, the additional scanned angle goes beyond the FoV of the imaging domain and hence contributes very little to the mode diversity. To further demonstrate the effect of FoV on the saturation of mode diversity, one may further extend the imaging domain to  $L_I = 12\lambda_0$ , which corresponds to FoV=126°. Fig. 6 shows the singular value distributions and interaction capacities for different scanning rates  $\varrho$ . In this case, while increasing the scanning rate from  $10^\circ/1\%$  to  $12^\circ/1\%$ , both the mode diversity and interaction capacity have more significant changes than those of Fig. 5. Instead, the saturation point changes to  $\varrho = 12^\circ/1\%$ , whose scanned angle range approximately corresponds to the 126° FoV. In summary, the mode diversity and interaction capacity are proportional to the scanning rate  $\varrho$ , and the FoV of the imaging domain determines the saturation point of  $\varrho$ .

Secondly, let us analyze the effect of the sampling number  $N$  on the imaging performance. As shown in Fig. 5, one has approximately 10 measurement modes with nonzero singular values, corresponding to a mode diversity of 10. Although the imaging domain is sampled into  $N = 100$  elements, most cannot be distinguished due to limited mode diversity. This indicates that it is unnecessary to sample the imaging domain into so many elements. Fig. 7 shows the singular value distributions and interaction capacities for different

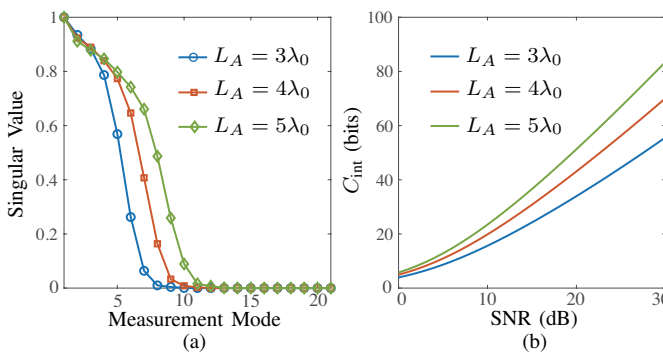


**FIGURE 8.** (a) Singular value distributions and (b) interaction capacities for different antenna aperture sizes corresponding to different beamwidths, while maintaining  $\varrho = 10^\circ/1\%$ ,  $L_I = 8\lambda_0$ , and  $N = 100$ .

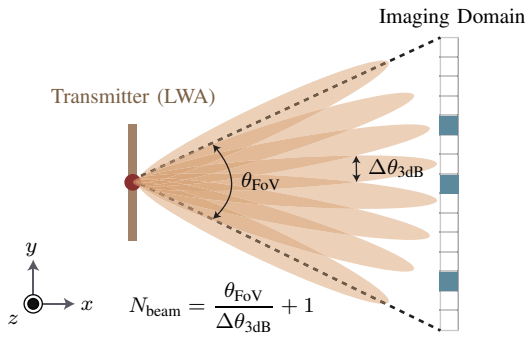


**FIGURE 9.** Computation of beam number in frequency-diverse imaging and sensing.

sampling numbers  $N$  while maintaining  $\varrho = 10^\circ/1\%$  and  $L_I = 8\lambda_0$ . As  $N$  reduces from 100 to 10, the mode diversity and interaction capacity do not change. As  $N$  further reduces to 9, the mode diversity and interaction capacity change a little. As  $N$  further reduces to 8, the mode diversity and interaction capacity exhibit more visible changes. So, 10 is the minimum sampling number to achieve the optimal imaging performance. This indicates that the minimum sampling number of the imaging domain can choose the mode diversity. This can be further employed to approximate the transversal resolution by dividing the imaging domain using the mode diversity. In this case, the transversal resolution is approximately  $8\lambda_0/10 = 0.8\lambda_0$ .

Finally, let us analyze the effect of beamwidth on the imaging performance. One may change the aperture size of the transmitting leaky-wave antenna to tune the beamwidth of the radiation beam. Fig. 8 shows the singular value distributions and interaction capacities for  $L_A = 3\lambda_0$ ,  $L_A = 4\lambda_0$ , and  $L_A = 5\lambda_0$ , which corresponds to beamwidths of  $16.8^\circ$ ,  $12.6^\circ$ ,  $10^\circ$ , respectively. Note that the mode diversity and interaction capacity increase as the beamwidth reduces. This can be understood by covering the fixed FoV using beams of different beamwidths. The beam with a narrower beamwidth allows more such beams to cover the FoV, leading to more diversity. So, one may define a beam number  $N_{beam}$  to indicate how many beams are allowed within the FoV of the

imaging domain. As illustrated in Fig. 9,  $N_{beam}$  is computed by

$$N_{beam} = \frac{\theta_{FoV}}{\Delta\theta_{3dB}} + 1, \quad (38)$$

where  $\theta_{FoV}$  denotes the angular range spanned by the imaging domain, and  $\Delta\theta_{3dB}$  is the half-power beamwidth of the radiation pattern. In the three cases of Fig. 8, i.e.,  $L_A = 3\lambda_0$ ,  $L_A = 4\lambda_0$ , and  $L_A = 5\lambda_0$ , the computed beam numbers are approximately 7, 9, and 11, respectively. These beam numbers show near parity with their corresponding mode diversity values (8, 10, and 12 across cases), maintaining a systematic difference of exactly -1 in all scenarios. This is because the mode diversity counts all the nonzero singular values, whereas the beam number within the FoV only counts the significant singular values corresponding to large interaction gains. The beam outside the FoV may interact negligibly with the imaging domain and exhibit very small singular values. It turns out that the beam number automatically discards the final small singular values when counting the measurement modes. Therefore, one may employ the beam number  $N_{beam}$  to denote the effective mode diversity of an antenna.

In frequency-diverse imaging and sensing, one is also interested in the spectrum efficiency, which characterizes how efficiently one uses the frequency spectrum for imaging and sensing. One may define such a spectrum efficiency,  $\eta_\omega$ , as

$$\eta_\omega = \frac{N_{beam}}{\Delta\omega/\omega_0}, \quad (39)$$

which indicates the effective mode diversity using per unit relative bandwidth. One should note that the definition of spectrum efficiency here differs from the usual definition in communication. By substituting (38) into (39), one can approximate  $\eta_\omega$  as

$$\eta_\omega \approx \frac{\theta_{FoV}}{\Delta\theta_{3dB}} \frac{1}{\Delta\omega/\omega_0} = \frac{\bar{\varrho}}{\Delta\theta_{3dB}}, \quad (40)$$

where  $\bar{\varrho} = \theta_{FoV}/(\Delta\omega/\omega_0)$  is called average scanning rate across the whole FoV. The physical meaning of (40) is straightforward. The spectrum efficiency is proportional to the average scanning rate, indicating how much bandwidth is required to scan the angular range of the FoV. The spectrum efficiency is also inversely proportional to the beamwidth, which indicates how many beams can be generated within the FoV. Although this average scanning rate differs from the scanning rate  $\varrho$  around the broadside in (37), one can still approximate  $\bar{\varrho}$  using  $\varrho$ . Therefore, once the scanning rate and beamwidth of a leaky-wave antenna are known, one can approximate the spectrum efficiency using (40).

In the design of frequency-diverse antennas, a large aperture with high directivity certainly realizes a large mode diversity. To compare different designs with different aperture sizes, one may further define a spectrum-aperture efficiency,  $\eta_{\omega A}$ , to indicate the effective mode diversity using per unit

relative bandwidth and per unit aperture. It is computed by

$$\eta_{\omega A} = \frac{\eta_\omega}{S_A/\lambda_0^2} = \frac{\bar{\varrho}\lambda_0^2}{\Delta\theta_{3dB} S_A}, \quad (41)$$

where  $S_A$  is the area of the antenna aperture. Since the directivity  $D$  is inversely proportional to the beamwidth, one may replace  $\Delta\theta_{3dB}$  of (41) with  $D$ , leading to

$$\eta_{\omega A} = \text{const} \cdot \frac{\bar{\varrho}D}{S_A/\lambda_0^2}, \quad (42)$$

where 'const' is a constant determined by the radiation pattern on the other plane. Notably, the spectrum-aperture efficiency has two contributions, where  $\bar{\varrho}$  indicates the spectrum usage, and  $D/(S_A/\lambda_0^2)$  denotes the directivity per unit aperture area. Suppose the radiation efficiency is also included from the system level. In that case, one may replace  $D$  by the gain  $G$  in (42) and define a total diversity efficiency for a 1-D frequency-diverse leaky-wave antenna. This total diversity efficiency,  $\eta_{\text{diversity}}$ , is

$$\eta_{\text{diversity}} = \frac{\bar{\varrho}}{180^\circ} \cdot \frac{G}{S_A/\lambda_0^2}, \quad (43)$$

which replaces 'const' in (42) with  $1/180^\circ$  to normalize the scanned angular range with respect to full space.

It should be noted that several additional parameters require consideration in practical implementation. For instance, the target-to-antenna distance also plays an important role. Increasing distance leads to greater transmission loss, reducing SNR while simultaneously decreasing FoV, both of which degrade sensing capacity. Additionally, insufficient isolation between the transmitter and receiver must be mitigated to prevent self-interference from compromising sensing capabilities.

In summary, when designing frequency-diverse antennas for imaging and sensing applications, it is essential to consider two key parameters based on the total diversity efficiency in (43), i.e., scanning rate and gain per unit aperture. Additionally, scanning angular range is also a critical factor because it directly impacts the maximum allowable FoV in various applications. Therefore, scanning rate, gain per unit aperture, and scanning angular range are the three main parameters that need to be addressed for optimal performance.

#### IV. Dispersion Engineering for Frequency-Diverse Antennas

As mentioned in the introduction, there are two distinct approaches to engineer the dispersion of frequency-diverse antennas, i.e., magnitude dispersion and phase dispersion. This review paper will focus on the latter. This type of frequency-diverse antenna features high-gain radiation beams directly steered by frequency. Such antennas are often referred to as *frequency-scanning antennas*. As evidenced in Sec. III-C, a high scanning rate is preferred to enhance the diversity of these beam-scanning antennas. This section will systematically introduce the fundamental principle of high-scanning-rate frequency-scanning antennas, and then review

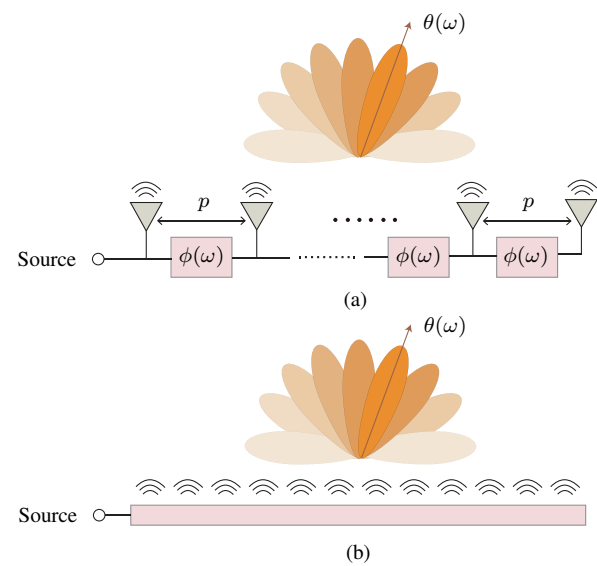


**FIGURE 10.** Architecture of (a) series-fed antenna array and (b) leaky-wave antenna as an extreme case of (a).

the latest development in this area. We will start with 1-D frequency-scanning antennas and extend them to 2-D cases.

#### A. 1-D High-Scanning-Rate Frequency-Scanning Antennas

Let us start with the general series-fed periodic antenna array in Fig. 10(a), which has many discrete radiators connected through phase-shifting components. The distance between the adjacent radiators is  $p$ , and each phase-shifting component provides a phase delay  $\phi(\omega)$ . The leaky-wave antenna in Fig. 10(b) can be regarded as an extreme case of (a) as the element distance  $p$  becomes electrically small (i.e.  $p \ll \lambda_0$ ) so that the whole structure is equivalent to a quasi-homogeneous artificial transmission line. In this case, the phase-shifting part and radiating part are merged. It should be noted that the antenna array in Fig. 10(a) assumes weak mutual coupling. Under conditions of strong mutual coupling, spurious radiation modes may emerge, degrading the radiation pattern and antenna gain while inducing significant port reflections. These combined effects would compromise sensing performance. While characteristic mode analysis could address such cases by manipulating global radiation modes with mutual coupling considerations [54], we maintain the weak coupling assumption here for illustrative simplicity.

According to the antenna array theory, the radiated beam angle,  $\theta(\omega)$ , satisfies

$$\sin \theta(\omega) = \frac{\phi(\omega)}{k_0 p} = \frac{\phi(\omega)c}{\omega p}, \quad (44)$$

where  $c$  is the speed of light in air. As the beam scans to the broadside at  $\omega_0$ , one has  $\theta(\omega_0) = 0$ . According to (44), the phase delay satisfies  $\phi(\omega_0) = 0$ . Let us consider the scanning rate around the broadside as defined in (37). By

substituting (44) into (37), one has

$$\varrho = \frac{c}{p} \frac{d\phi}{d\omega}. \quad (45)$$

One may further substitute the group delay  $\tau = d\phi/d\omega$  into (45), leading to

$$\varrho = \frac{c\tau}{p}. \quad (46)$$

In the case of leaky-wave antennas in Fig. 10(b), the phase delay is computed by  $\phi(\omega) = \beta(\omega)p$ , where  $\beta$  is the propagation constant of the equivalent homogeneous transmission line. By substituting  $\phi(\omega) = \beta(\omega)p$  into (45), one obtains

$$\varrho = c \frac{d\beta}{d\omega} = \frac{c}{v_g}, \quad (47)$$

where  $v_g = d\omega/d\beta$  is the group velocity of the leaky-wave transmission line.

The formula (46) and (47) describe the essence of enhancing the scanning rate of series-fed antenna arrays and leaky-wave antennas, respectively. In the case of a series-fed antenna array, the scanning rate is proportional to  $\tau/p$ , that is, the group delay per unit distance. In the case of leaky-wave antennas, the scanning rate is inversely proportional to the group velocity  $v_g$ . Following this, one may classify the current scanning rate enhancement techniques into three categories: large-delay feeding technique, slow-group-velocity feeding technique, and coupled-resonator feeding technique. We will introduce and review these three categories as follows.

### 1) Large-Delay (LD) Feeding Technique

The large-delay feeding technique follows the indication of (46), that is, the scanning rate is proportional to the group delay per unit distance ( $\tau/p$ ). So, one either increases the group delay  $\tau$  or reduces the element distance  $p$  to enhance the scanning rate.

The first try on increasing the group delay is explored in [42], where complementary microstrip-slotline stubs are inserted into the series-fed antenna array to increase the scanning rate. The complementary microstrip-slotline stub is an all-pass element, which exhibits a large group delay and a flat magnitude across the whole frequency band. Therefore, its insertion only affects the group delay and has little perturbation to the magnitude and impedance matching of the original series-fed antenna array. Such an antenna exhibits a scanning rate of  $4.5^\circ/1\%$ . This idea is later extended in [44], where the complementary microstrip-slotline stub is slightly tuned to provide a large delay, meanwhile maintaining a small leaky radiation. The large-delay feeding line and radiator merge as one in [44]. Such an antenna is able to scan  $30^\circ$  within 8% bandwidth ( $\bar{\varrho} = 3.8^\circ/1\%$ ). In [74], researchers employ a filtering structure to increase the group delay and enhance the scanning rate. The designed antenna is able to scan  $40^\circ$  within 5% bandwidth ( $\bar{\varrho} = 8^\circ/1\%$ ).

Reduction of element distance or element period,  $p$ , has also been explored in various reported works. In [75], meander microstrip line is employed for the first time to reduce the radiator distance of a series-fed slot array antenna. The resulting antenna scans  $50^\circ$  within 25% bandwidth ( $\bar{\varrho} = 2^\circ/1\%$ ). In [50], coupled meandered-line structure is proposed to scan  $120^\circ$  within 17% bandwidth ( $\bar{\varrho} = 7.1^\circ/1\%$ ). In [76], a meandered composite-right-left-handed (CRLH) transmission line is employed to reduce the element period. The designed antenna scans  $80^\circ$  within 8.3% bandwidth ( $\bar{\varrho} = 9.6^\circ/1\%$ ). One should note that, although the meander line increases the scanning rate, it leads to a wider antenna width.

In summary, the large-delay feeding technique employs group delay enhancement and element distance reduction approaches. According to the reported works, the realized scanning rates are usually below  $10^\circ/1\%$ .

### 2) Slow-Group-Velocity (SGV) Feeding Technique

As  $p$  gets very small, the series-fed antenna array becomes a quasi-homogeneous leaky-wave line. In this case, one employs the slow-group-velocity feeding technique following the indication of (47), that is, the scanning rate is inversely proportional to the group velocity  $v_g$ . Therefore, to realize a high-scanning-rate leaky-wave antenna, the dispersion curve in the  $\omega - \beta$  diagram should have a tiny slope across the fast-wave region. Most leaky-wave antennas radiate waves through space harmonics, which is realized by periodically modulating a slow-wave transmission line. Such a modulation operation is equivalent to shifting the dispersion curve from the slow-wave region to the fast-wave region without changing the slope. Therefore, to realize slow-group-velocity leaky-wave radiation, one should first design a slow-group-velocity slow-wave feeding line and modulate the line shape periodically to generate leaky-wave radiation.

The most popular approaches to achieve a slow group velocity are the employment of spoof surface plasmon polaritons (SSPP), also known as a corrugated Goubau line in some other works. SSPP and Goubau line refer to the same structure with different terminologies. SSPP mimics surface plasmon polaritons (SPP) at optical frequencies with similar characteristics. As the frequency is close to the surface plasmon frequency, SPP behaves like quasi-particles, which naturally exhibit very slow group velocities. Similarly, SSPP exhibits a small group velocity when the frequency gets close to the spoof surface plasmon frequency, which is also called the cutoff frequency from the transmission line perspective. This idea was employed for the first time to enhance the scanning rate in [43], where high-density slots are cut on the top plane of a substrate integrated waveguide (SIW) to produce an upper cutoff frequency similar to the SSPP effect. By subsequently modulating the slot width periodically to shift the dispersion curve close to the cutoff frequency to the fast-wave region, one designs

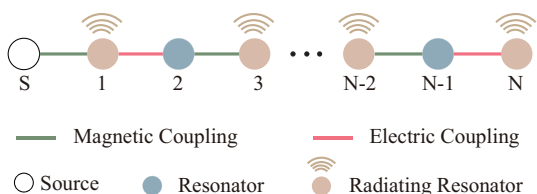


FIGURE 11. Architecture of coupled-resonator frequency-scanning array antenna.

a high-scanning-rate leaky-wave antenna, which scans  $35^\circ$  within 3% bandwidth ( $\bar{\varrho} = 12^\circ/1\%$ ). This design was later improved by using double-side slots in [34] and [77], which extends the scanning angular range to  $70^\circ$  over 4.9% bandwidth ( $\bar{\varrho} = 14.4^\circ/1\%$ ) and  $120^\circ$  over 9% bandwidth ( $\bar{\varrho} = 13.3^\circ/1\%$ ), respectively. In [78], a linear scanning technique was proposed for high-scanning-rate leaky-wave antennas, which allows the designed antenna to linearly scan  $51^\circ$  over 9% bandwidth ( $\bar{\varrho} = 5.7^\circ/1\%$ ). In [79], a dual-beam technique based on SSPP structure was proposed for high-scanning-rate leaky-wave antennas, which support two beams scanning  $66^\circ$  over 9% bandwidth ( $\bar{\varrho} = 7.3^\circ/1\%$ ).

Wide scanning angular range, denoting the maximum allowable FoV of the imaging domain, is another key design factor besides high scanning rate. Slow group velocity usually occurs close to the cutoff frequency, which may cause strong reflection at the stopband and limit the scanning angular range. To overcome this drawback, a glide-symmetry corrugated Gouba line [45] was proposed to suppress the stopband while maintaining a slow-group-velocity dispersion curve. The designed leaky-wave antenna scans  $145^\circ$  over 7% bandwidth ( $\bar{\varrho} = 20.7^\circ/1\%$ ). In [80], a microstrip SSPP leaky-wave antenna was designed to scan  $172^\circ$  over 22.4% bandwidth ( $\bar{\varrho} = 7.7^\circ/1\%$ ). In [81], a full-space-scanning SSPP leaky-wave antenna was proposed to extend the scanning angle range to  $180^\circ$  over 24% bandwidth ( $\bar{\varrho} = 7.5^\circ/1\%$ ). Recently, an interesting design [82] exploring the combination of a high-Q resonator and a periodic leaky-wave antenna has been reported to scan  $180^\circ$  over 18.5% bandwidth ( $\bar{\varrho} = 9.7^\circ/1\%$ ).

In summary, the slow-group-velocity feeding technique has significantly improved the scanning rate and scanning angular range. However, as the scanning rate increases, the total efficiency of leaky-wave antennas usually drops. For example, the measured efficiency of [45] is only 30%. The trade-off between dispersion and loss limits the leaky-wave antenna from further enhancing its scanning rate.

### 3) Coupled-Resonator (CR) Feeding Technique

The coupled-resonator feeding technique is proposed to overcome the low efficiency of high-scanning-rate leaky-wave antennas. Fig. 11 shows the architecture of a coupled-resonator frequency-scanning antenna. Instead of using a wideband transmission line to feed radiators in Fig. 10, this new architecture couples many high-Q resonators to

form a narrowband channel to feed all the radiators. By squeezing the spectrum into a narrow band, the transmission phase changes sharply with frequency within this narrow band, and the employment of a high-Q resonator significantly suppresses the loss and enhances efficiency. This idea was proposed for the first time by [53], which exactly employs the architecture in Fig. 11. A bulky waveguide cavity is used as the resonator, and alternating magnetic/electric couplings allow the beam to scan across the broadside within the operational frequency band. Slots are cut on the odd-number cavity to produce radiation. Coupling matrix theory is employed to synthesize the required coupling coefficients. Such a new feeding technique allows the antenna to scan  $66^\circ$  over 1.25% bandwidth with an extremely high scanning rate ( $\bar{\varrho} = 53^\circ/1\%$ ). Meanwhile, the measured total efficiency maintains 70% on average.

Although the coupled-resonator frequency-scanning antenna in [53] has both an extremely high scanning rate and a high efficiency, it is bulky and is unsuitable for low-profile applications. A coupled-patch array antenna [54] was later proposed for planar implementation. A codesign technique based on coupling matrix theory and characteristic mode analysis was proposed for the first time in this work. The designed planar frequency-scanning antenna can scan  $73^\circ$  over 2.8% bandwidth ( $\bar{\varrho} = 26^\circ/1\%$ ) and maintain a good efficiency of 60% on average. The scanning angular range was later improved by a 12<sup>th</sup>-order design in [17], which can scan  $93^\circ$  over 4% bandwidth ( $\bar{\varrho} = 23^\circ/1\%$ ). This design was applied to multi-target wireless localization and respiration monitoring for the ISAC application. The most recent planar coupled-resonator design [55] in this area has pushed the scanning rate record up to  $70^\circ/1\%$  and maintains a good efficiency of 60% on average.

In summary, the coupled-resonator feeding technique has increased the scanning rate to a new high record while maintaining good efficiencies. However, the scanning angular range is still limited below  $100^\circ$  according to all reported works. Besides, the aperture size and gain are also limited due to the complexity in designing and tuning high-order coupled-resonator structures. Therefore, substantial research efforts are still required to simultaneously realize a high scanning rate, broad angular coverage, and high gain in a single antenna.

## B. 2-D Spatial-Diversity Extension

The above section has systematically introduced the design of 1-D high-scanning-rate antennas, which can steer radiation beams on a 1-D plane via frequency variations. However, in some applications, 1-D beam scanning is insufficient, and one must seek 2-D beam scanning capability for frequency-scanning antennas. Although 2-D leaky-wave antennas have been extensively studied, generating a frequency-controlled beam that can independently scan two planes is challenging.

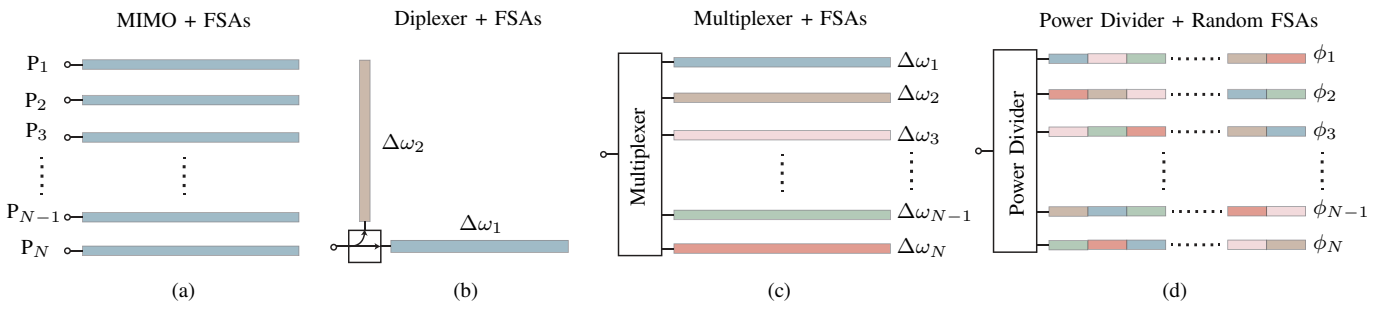


**FIGURE 12.** Various techniques to extend the frequency diversity to 2-D: (a) MIMO plus frequency scanning antennas (FSAs) [35], [83]; (b) diplexer plus two perpendicularly-oriented FSAs [84]; (c) multiplexer plus multiple FSAs [85]; (d) power divider plus FSAs with randomly encoded phases [36], [71].

Fig. 12 provides four state-of-the-art techniques to extend the spatial diversity of 1-D frequency-scanning antennas to a 2-D space. The most commonly used technique is to employ a MIMO system to connect multiple 1-D frequency-scanning antennas [35], [83], as shown in Fig. 12(a). The frequency-scanning antennas scan the beam along the horizontal plane via different frequencies, and MIMO scans the beam along the vertical plane via digital beamforming techniques. So this technique can independently scan beams along two planes. The principal limitation stems from the prohibitive implementation costs inherent in MIMO system architectures, necessitating the development of single-port extension methodologies to mitigate hardware expenditure.

Fig. 12(b) provides a single-port extension approach using a diplexer to connect two perpendicularly-oriented 1-D frequency-scanning antennas [84]. The diplexer divides the whole frequency band into two sub-bands, one used to monitor the horizontal plane and the other used to scan the vertical plane. This technique can track a single object on a 2-D plane in real-time. However, if there are multiple objects or objects with complicated shapes, the solution is not unique due to the limited information provided by only two antennas.

Fig. 12(c) proposes an improved version of (b), where the diplexer is replaced by a multiplexer and more 1-D frequency scanning antennas are employed [85]. The whole frequency band is divided into many sub-bands,  $\Delta\omega_1, \Delta\omega_2, \dots, \Delta\omega_N$ , each of which is used by a 1-D frequency-scanning sub-antenna for horizontal beam scanning. This architecture of (c) is similar to MIMO in (a), where each sub-antenna can work independently. One can achieve spatial diversity on the vertical plane by controlling different sub-bands. Therefore, this architecture employs the tool of pure frequency to achieve spatial diversity in 2-D space. It has been successfully demonstrated by [85] that such an antenna can detect objects on a 2-D plane in real-time. However, the multiplexer is very difficult to design, especially as the channel number is large. The usage of enormous spectrum resources is another drawback of this technology.

Fig. 12(d) replaces the multiplexer of (c) with a power divider to overcome its design complexity. However, realizing spatial diversity on the vertical plane becomes a big

challenge. If all the sub-antennas are the same, they will form a fixed narrow beam on the vertical plane, which does not scan to produce spatial diversity on the vertical plane. To create spatial diversities on the vertical plane, the works in [36], [71] apply a random phase coding technique to each sub-antenna. Since each sub-antenna is encoded with different phase distributions along the horizontal axis, their frequency dependences are also randomly different. This leads to a low correlation between each sub-antenna across the frequency band. As evidenced by [36], [71], such an architecture can realize 2-D microwave imaging and hand gesture recognition in real-time. The only drawback of this technology lies in the widespread radiation pattern due to the random phase distributions. This may lead to a low SNR in some applications. Therefore, a tradeoff between diversity and SNR has to be considered in specific applications.

In summary, all four techniques in Fig. 12 have their own advantages and drawbacks. According to various application scenarios, one may choose the proper technique accordingly. Additionally, these 2-D extension techniques in Fig. 12 can potentially support 3-D frequency-diverse imaging and sensing. This has been experimentally demonstrated in the case of MIMO frequency-diverse antennas in Fig. 12(a) [35]. It should be emphasized that high-scanning-rate frequency-diverse antennas preserve superior transversal resolution, although their range resolution remains fundamentally limited compared to conventional broadband imaging systems due to the inverse relationship between distance resolution and system bandwidth.

### C. Comparison and Discussion

The above sections have introduced the dispersion engineering techniques for frequency-scanning antennas. Let us summarize and compare these techniques from an application and information-theoretic perspective.

From the application perspective, scanning angular range and scanning rate are primarily of concern. The scanning angular range determines the maximum allowable FoV of application scenarios. So, a wide angular range is always preferred to be adapted to various applications. The scanning rate determines the spectrum occupation for imaging and sensing. A higher scanning rate, requiring fewer

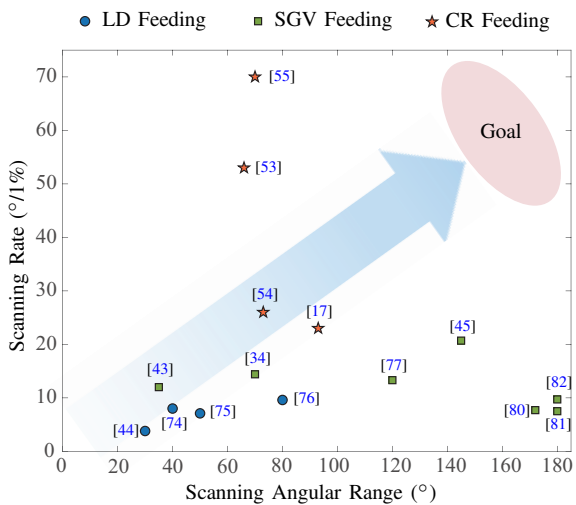


FIGURE 13. Scanning rate and scanning angular range comparison of some typical frequency-scanning antennas.

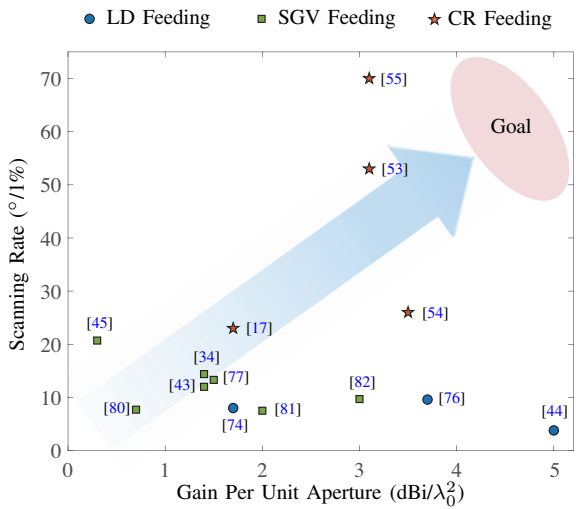


FIGURE 14. Scanning rate and gain per unit aperture comparison of some typical frequency-scanning antennas.

spectrum resources, is highly demanded. Fig. 13 compares typical techniques reported to date according to scanning rate and scanning angular range. Note that the slow-group-velocity feeding technique achieves a wide scanning angular range, up to  $180^{\circ}$ , yet remains limited by a scanning rate constrained below  $25^{\circ}/1\%$ . The coupled-resonator feeding technique realizes very high scanning rates, up to  $70^{\circ}/1\%$ , but maintains a constrained scanning angular range below  $100^{\circ}$ . One may explore the combination of coupled-resonator feeding and slow-group-velocity feeding techniques to reach the ultimate goal of both high scanning rate and wide scanning angular range in the future. The work in [82] has started this exploration.

From the information-theoretic perspective, the total diversity efficiency in (43) indicates the number of effective measurement modes provided by unit bandwidth and unit aperture. According to (43), the total diversity efficiency is

determined by two parameters, i.e., scanning rate and gain per unit aperture. Fig. 14 compares all the techniques using these two parameters. Note that most of slow-group-velocity feeding techniques suffer from poor gain-per-unit-aperture performance. The coupled-resonator feeding technique is the most promising technique for reaching a high scanning rate and gain per unit aperture.

In summary, ideal frequency-scanning antennas should achieve high scanning rate, wide scanning angular range, and high gain per unit aperture simultaneously. However, the current three techniques cannot optimize all three metrics concurrently. This indicates great opportunities in the design of frequency-scanning antennas in the future.

## V. Applications of Frequency-Diverse Imaging and Sensing

### A. Review of Recent Progress

Frequency-diverse imaging and sensing are widely applied in various domains. The early-stage applications are mostly broadband due to the bandwidth requirement of metamaterial-based antennas. In [29], computational imaging based on frequency-diverse metamaterials was proposed. It needs a wide frequency band (17.5–26.5 GHz, with 41% bandwidth) to generate enough measurement modes. The aperture was later enlarged to  $2.1 \times 2.1 \text{ m}^2$  using 96 metamaterial antennas for a security screening application [86], [87]. Notably, this imaging system can capture a moving human at 7 Hz. But it still requires 41% frequency bandwidth to have enough diversity. Recently, researchers integrated the transmitter and receiver in a single low-profile metasurface-based reflectarray for microwave imaging [88], which requires 82% frequency bandwidth.

Synthetic aperture radar (SAR) frequency-diverse imaging was also explored using metamaterial antennas within 17.5–20.3 GHz [89]. It demonstrated that such a frequency-diverse system can achieve comparable image qualities to a traditional system, proving its potential to be applied in future SAR platforms. In [90], a broadband frequency-diverse metasurface was proposed for through-wall radar imaging. It can reconstruct moving objects at 100 Hz from a single-shot measurement. Many other applications of metamaterial-based imaging can be found in the review paper [38].

Since the development of high-scanning-rate antennas [42]–[45], frequency-diverse imaging can be realized within a narrow frequency band, which not only saves the spectrum resource but also reduces the sampling rate requirement for ADC in the baseband system. As demonstrated in [34], a high-scanning-rate leaky-wave antenna employing 5% bandwidth only can achieve comparable imaging performance to the metamaterial antennas of [29] using 41% bandwidth.

The proposal of extremely-high-scanning-rate frequency-scanning antennas [53]–[55] further fits them to the wireless communication frequency band and hence promotes their applications to ISAC. In [91], the extremely-high-scanning-

rate frequency-scanning antenna, scanning  $66^\circ$  within 1.25% bandwidth, is applied to direction-of-arrival (DoA) estimation for industrial internet of things (IIoT) applications. In [17], a wireless sensing application was proposed by using an extremely-high-scanning-rate antenna ( $\bar{\varrho} = 25.8^\circ/1\%$ ) working in the indoor wireless communication band. Such a system is demonstrated for multitarget localization, respiration detection, and surrounding interference mitigation. This idea was recently applied to a MIMO frequency-diverse antenna [83] for multitarget localization in 2-D space and real-time heartbeat rate monitoring. This work demonstrates a millimeter-wave (60-64 GHz) MIMO coupled-resonator antenna system combining vertical frequency scanning with  $3\text{Tx} \times 4\text{Rx}$  digital beamforming for 2-D multitarget localization. Integrated with an FMCW radar, the prototype experimentally achieves simultaneous spatial localization and sub-movement detection (including heart rate monitoring) through hybrid analog-digital beam steering.

Hand gesture recognition has also been explored recently using cavity-backed frequency-diverse antennas [33] and random-phase-coded high-scanning-rate antennas [71]. Sensing capacity formula in (31) is employed by [33] to optimize the antennas, and a convolutional neural network (CNN) is used to identify 10 distinct hand gestures. In [71], an SSPPs frequency-diverse antenna was demonstrated that simultaneously enables high-resolution frequency-diverse imaging and CNN-powered gesture recognition (36 classes) with minimal bandwidth.

Integrated backscattering communication and sensing [16] has been demonstrated recently using the extremely-high-scanning-rate antenna in [55]. It explored an integrated system combining inverse scattering and compressive sensing to enable simultaneous tag localization, identification, and backscatter communication in cluttered environments. By modulating tags between open/short-circuit states to separate structural and antenna modes, the system achieves scatterer sensing (via structural mode) and tag identification (via antenna mode) while maintaining communication in cluttered environments. ISAC using full-space high-scanning-rate leaky-wave antennas was also explored recently in [56]. It demonstrated a compact ISAC platform based on a full-space-scanning leaky-wave antenna for simultaneous wireless sensing (i.e., static imaging, multitarget localization, and respiration monitoring) and reliable communication (21 dB SNR), validated as a cost-effective solution for IoT/healthcare applications.

In summary, frequency-diverse imaging and sensing has undergone a transformative evolution, progressing from its nascent applications in broadband imaging to cutting-edge implementations in narrowband ISAC. Looking ahead, the ongoing breakthroughs in extremely-high-scanning-rate antenna technology are poised to catalyze the advent of novel applications across diverse domains, ultimately redefining the boundaries of electromagnetic wave manipulation for next-generation imaging and sensing systems.

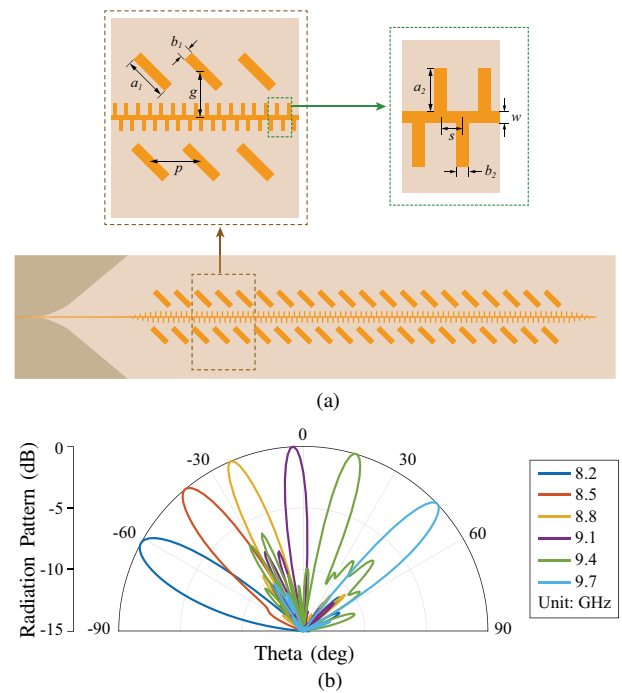


**FIGURE 15.** (a) Configuration and (b) radiation patterns of the leaky-wave antenna for frequency-diverse imaging and sensing ( $a_1=10$ ,  $b_1=2.5$ ,  $a_2=2.5$ ,  $b_2=0.76$ ,  $p=10$ ,  $g=8.9$ ,  $s=0.625$ , unit: mm).

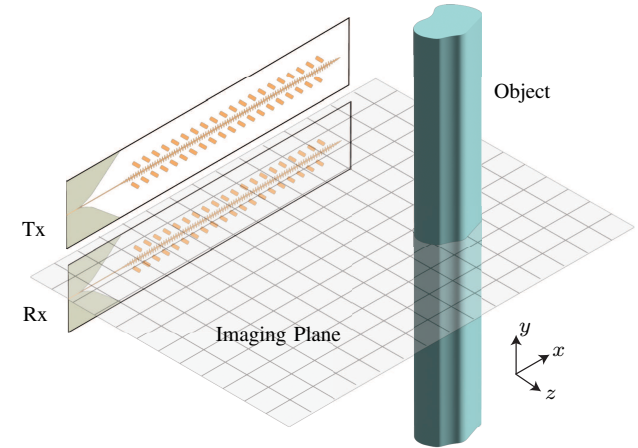


**FIGURE 16.** Microwave near-field imaging of object contour on  $xz$ -plane using high-scanning-rate leaky-wave antennas as both transmitter and receiver.

### B. Illustrative Examples: Imaging and Position Tracking

To better illustrate the applications of frequency-diverse imaging and sensing, we provide several examples covering the workflow from antenna design to practical implementation.

The first example presents an imaging application utilizing a glide-symmetry high-scanning-rate leaky-wave antenna, as illustrated in Fig. 15 and designed according to [45]. The antenna achieves beam scanning from  $-62^\circ$  to  $47^\circ$  within 8.2–9.7 GHz, with  $0^\circ$  defining broadside direction. The average scanning rate is  $\bar{\varrho} = 6.4^\circ/1\%$  and the average gain is about 10 dBi. The imaging configuration (Fig. 16) employs

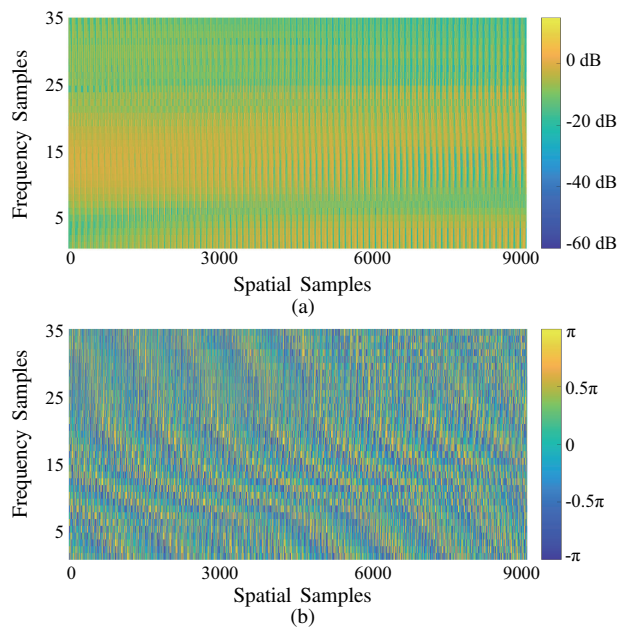


**FIGURE 17.** (a) Magnitude and (b) phase of the measurement matrix in the imaging scenario of Fig. 16.

two identical leaky-wave antennas located at the origin of the  $xy$ -plane, functioning as transmitter and receiver. Imaging targets include a rod object oriented along the  $y$ -axis, with the objective of 2-D contour reconstruction.

The imaging domain is chosen as a 2-D rectangular region on the  $xz$ -plane, where  $x \in [-180 \text{ mm}, 180 \text{ mm}]$  and  $z \in [60 \text{ mm}, 160 \text{ mm}]$ . First, one discretizes the imaging domain into 9000 pixels, each occupying a  $2 \text{ mm} \times 2 \text{ mm}$  area. One subsequently discretizes the operational frequency band into 35 samples. Then one formulates the forward linear problem in (11), which is reproduced here as

$$\mathbf{H}\varepsilon = \nu, \quad (48)$$

where the measurement matrix  $\mathbf{H}$  is constructed by following (12) and the resultant values are plotted in Fig. 17. Applying SVD to the measurement matrix computes the singular value distribution and interaction capacities in Fig. 18. Notably, singular values become negligible after 30 modes, demonstrating the adequacy of 35 frequency samples.

The inverse problem presented in (48) exhibits ill-posedness. However, under sparsity constraints, this problem admits reformulation through  $\ell_1$ -norm optimization, i.e.

$$\min_{\varepsilon} \|\varepsilon\|_1, \text{ s.t. } \mathbf{H}\varepsilon = \nu, \quad (49)$$

where  $\|\cdot\|_1$  denotes the  $\ell_1$ -norm. While various compressive sensing algorithms are applicable to (49), this work employs the two-step iterative shrinkage thresholding (TwIST) algorithm [92]. Fig. 21 presents reconstruction results for one and two square rods, where the close agreement between recovered and actual contours demonstrates the efficacy of frequency-diverse imaging using high-scanning-rate leaky-wave antennas.

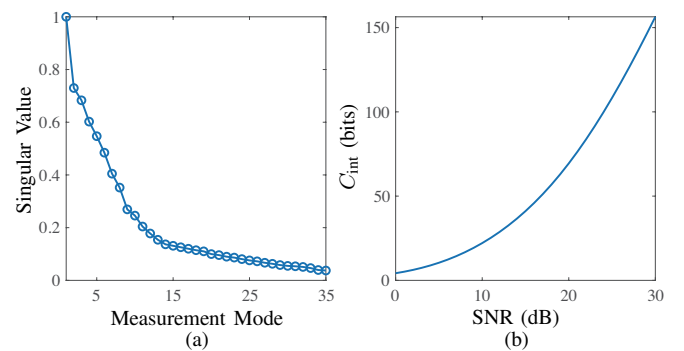


**FIGURE 18.** (a) Singular value distributions and (b) interaction capacities for the measurement matrix in Fig. 17.

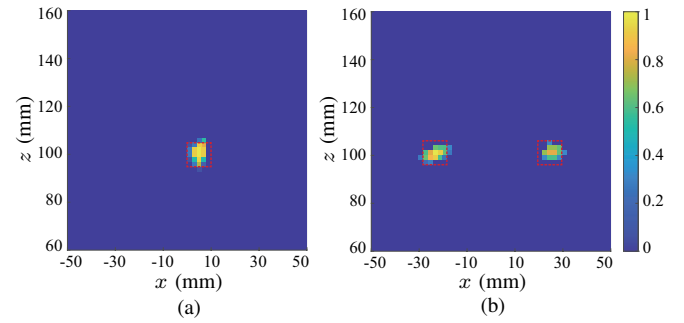


**FIGURE 19.** Imaging results of (a) one square rod and (b) two square rods. The red rectangles denote the true objects.

For applications prioritizing transversal plane positioning over shape accuracy, Fig. 20(a) shows a 2-D position tracking system using two orthogonally placed, high-scanning-rate leaky-wave antennas. Operating in distinct bands (8.2–9.4 GHz and 6.2–7.4 GHz), they independently scan the  $yz$ - and  $xz$ -planes, combined via a diplexer. The fabricated prototype appears in Fig. 20(b), with design details in [84]. A broadband horn antenna serves as the receiver in this single-input-single-output system capable of 2-D position tracking. Experimental demonstrations with a  $10 \text{ mm} \times 10 \text{ mm}$  metal sheet placed 100 mm from the antenna plane show excellent agreement between recovered and actual positions, as evidenced by Fig. 21.

In summary, high-scanning-rate leaky-wave antennas enable frequency-diverse imaging systems to both reconstruct rod scatterer contours and accurately track object positions on the transversal plane.

### C. Illustrative Examples: Human-Target Localization and Vital-Sign Monitoring

The development of extremely-high-scanning-rate frequency-scanning antennas significantly enhances frequency-diverse sensing capabilities for ISAC applications. As illustrative examples, we present human-target sensing and vital-sign monitoring at both Wi-Fi frequencies and millimeter-wave frequencies.

We employ a coupled-resonator frequency-scanning antenna for illustration, as shown in Fig. 22, which is de-

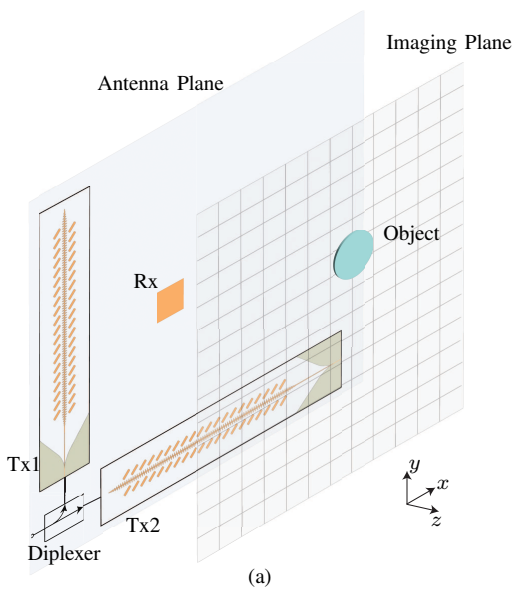


**FIGURE 20.** Object tracking on 2-D  $xy$ -plane using two perpendicularly placed leaky-wave antennas and one diplexer: (a) imaging setup; (b) fabricated prototype of the antennas.

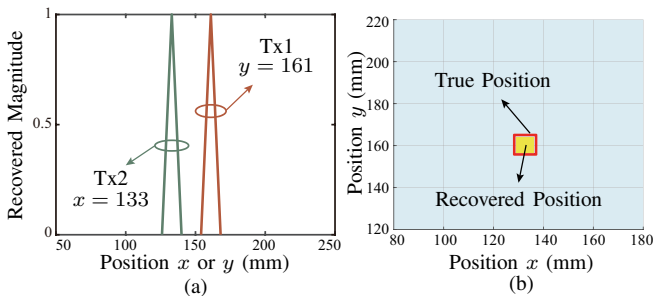


**FIGURE 21.** Recovered position of a metal sheet on (a)  $x$ -axis and  $y$ -axis, and (b) 2-D  $xy$ -plane.

signed using the codesign of characteristic mode analysis and coupling matrix method [54]. The antenna comprises twelve quarter-wavelength resonant patches coupled through alternating magnetic windows and electric gaps. More details regarding the design method can be found in [54]. This coupled-resonator antenna is specially designed to cover the Wi-Fi frequency at 5.8 GHz for the ISAC application. Fig. 23

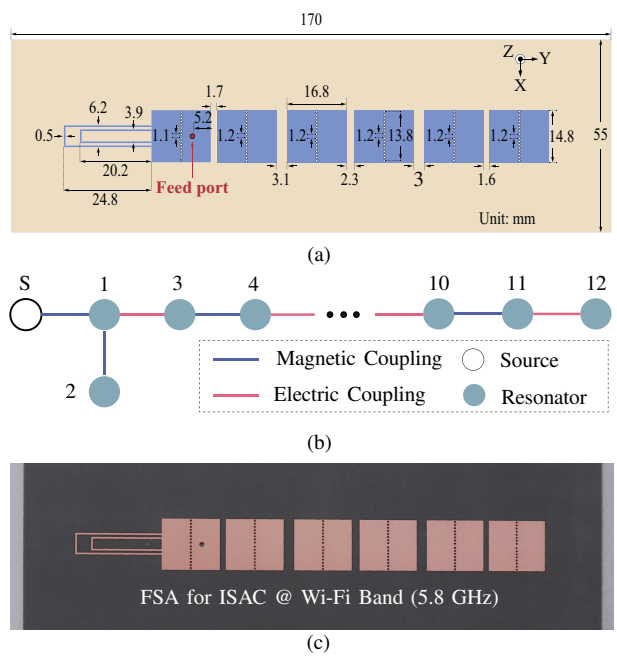


**FIGURE 22.** (a) Configuration, (b) coupling topology, and (c) fabricated prototype of the extremely-high-scanning-rate coupled-resonator frequency-scanning antenna (FSA) for ISAC at Wi-Fi frequency band.

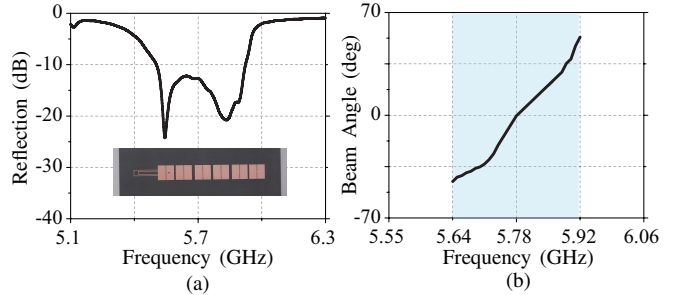


**FIGURE 23.** (a) Measured reflection response and beam angle versus frequency of the coupled-resonator frequency-scanning antenna.

shows the measured reflection response and beam angle versus frequency. The antenna achieves beam scanning from  $-45^\circ$  to  $54^\circ$  within the operational frequency band 5.64–5.92 GHz. The average scanning rate is  $\bar{\varrho} = 20.4^\circ/1\%$ .

Coupled-resonator frequency-scanning antennas have proven effective for human-target localization and respiration monitoring in indoor communication bands [17]. We now experimentally demonstrate this capability at Wi-Fi frequencies. The sensing system configuration, shown in Fig. 24, utilizes the designed frequency-scanning antenna as the transmitter and a standard monopole Wi-Fi antenna as the receiver, with a vector network analyzer (VNA) functioning as the transceiver. When a human target is present, respiratory-induced abdominal displacement modulates the reflected signal. Significant signal variation thus indicates both human presence and strong respiration activity.

The frequency-scanning antenna enables angular localization by detecting reflected signal variations across different

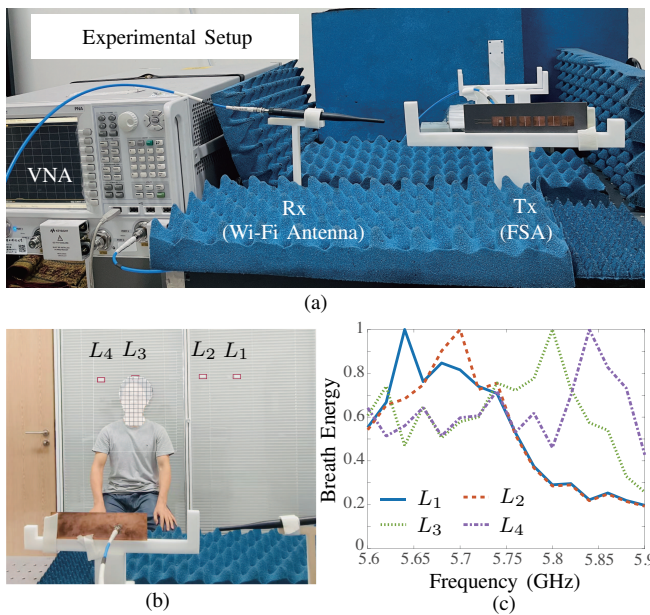


**FIGURE 24.** (a) Experimental setup for human target localization and respiration monitoring; (b) illustration of the target at different locations ( $L_1$ ,  $L_2$ ,  $L_3$ ,  $L_4$ ); (c) breath energies versus frequency when the target is at different locations. The target is about 1.5 m away from the antenna.

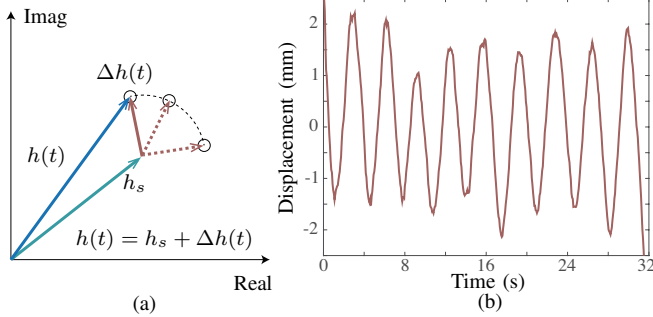


**FIGURE 25.** (a) Movement of received signal in complex plane due to respiration; (b) extracted abdomen displacement for respiration monitoring.

frequencies. Figs. 24(b) and (c) demonstrate this capability, showing human targets at different locations ( $L_1$  to  $L_4$ ) and their corresponding breath energy responses versus frequency. The observed peak shifts in breath energy precisely track target movement, consistent with the antenna's beam scanning characteristics. Following localization, respiration monitoring is achieved by analyzing abdominal displacement, as presented in Fig. 25. The received complex signal comprises both static ( $h_s$ ) and dynamic ( $\Delta h(t)$ ) components (Fig. 25(a)), where the dynamic phase information enables abdominal motion extraction (Fig. 25(b)). Clear periodic respiration signals are successfully observed.

Beyond microwave-frequency applications, we also provide a millimeter-wave implementation using 60 GHz MIMO radar with coupled-resonator frequency-scanning antennas (Fig. 26). This system achieves 2-D beam scanning and heartbeat monitoring through vertical plane beam steering

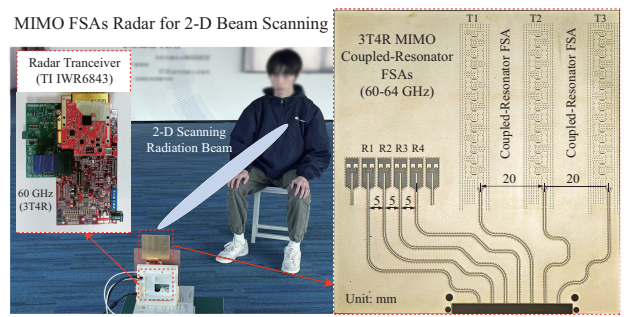


**FIGURE 26.** Millimeter-wave MIMO coupled-resonator frequency-scanning antennas for 2-D localization and heartbeat rate monitoring.

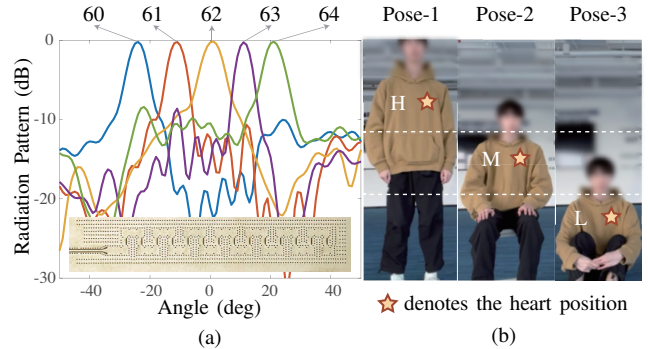


**FIGURE 27.** (a) Radiation patterns of the coupled-resonator frequency-scanning antenna at 60 GHz, 61 GHz, 62 GHz, 63 GHz, and 64 GHz; (b) detection of three poses via a vertically scanned beam positioned at high, middle, and low levels.

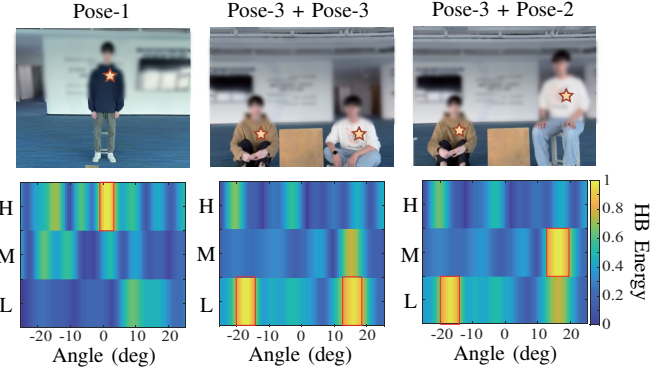


**FIGURE 28.** Localization and pose detection of multiple targets across three cases.

via coupled-resonator antennas and horizontal plane scanning using a 3Tx4Rx MIMO array with digital beamforming. The combined architecture enables independent 2-D transversal plane beam control.

The coupled-resonator frequency-scanning antenna is designed following the methodology in [53], [55]. Its beam scanning characteristics across the 60-64 GHz operational band are shown in Fig. 27(a), demonstrating a scanning range from  $-25^\circ$  to  $22^\circ$  with an average scanning rate of  $\bar{\varrho} = 7.3^\circ/1\%$ . Fig. 27(b) demonstrates pose identification capabilities for three scenarios: standing (pose-1), sitting (pose-2), and sitting/lying on the ground (pose-3)

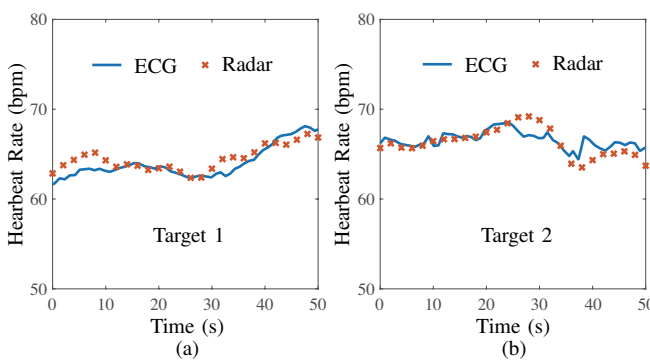


**FIGURE 29.** Heartbeat rate monitoring of two targets using the designed radar and ECG: (a) target 1; (b) target 2. The unit of heartbeat rate is beats per minute (bpm).

through vertical zone detection (H/M/L). Fig. 28 presents three experimental cases validating the system's horizontal localization and pose detection performance. Similar to breath energy detection in Fig. 24, we utilize heartbeat energy, obtained by filtering signal power within the cardiac frequency band, for 2-D transversal plane localization. The MIMO frequency-scanning antennas enable simultaneous horizontal localization and pose identification for two targets. Following localization, heartbeat rate extraction is achieved as shown in Fig. 29, with a strong correlation between radar and electrocardiogram (ECG) signals confirming system viability.

In summary, extremely-high-scanning-rate frequency-scanning antennas allow frequency-diverse sensing systems to localize multiple human targets while simultaneously monitoring their vital signs.

## VI. Conclusion and Outlook

This paper has systematically introduced frequency-diverse imaging and sensing, beginning with fundamental principles and progressing to cutting-edge developments in dispersion engineering for high-scanning-rate antennas and various novel applications. The electromagnetic-information theory has been presented to provide a design guideline for frequency-diverse antennas. Notably, the total diversity efficiency was derived as a clear indicator for the design of frequency-scanning antennas. Various scanning rate enhancement techniques have been reviewed and compared, and the 2-D spatial diversity extension technique was also discussed. Various applications were reviewed, progressing from nascent applications in broadband imaging to cutting-edge implementations in narrowband ISAC. Four application examples are finally provided to illustrate the frequency-diverse imaging and sensing.

Looking ahead, numerous challenges and opportunities exist in this rapidly evolving field, which are outlined and discussed below.

### 1) Frequency-Diverse Antennas:

Ideal frequency-diverse antennas should achieve high scanning rates, wide angular ranges, and gain simultaneously.

However, current techniques cannot optimize all three metrics concurrently. Fig. 13 shows such a trade-off. The slow-group-velocity feeding technique provides broad angular coverage but limited scanning rates, while the coupled-resonator feeding approach delivers extremely high scanning rates but a very narrow angular range. Meanwhile, Fig. 14 reveals that the large-delay feeding technique offers superior aperture efficiency but limited scanning rates. These complementary strengths suggest promising opportunities for hybrid designs, as preliminarily explored in [82], which combines coupled resonators with periodic leaky-wave structures from slow-group-velocity and large-delay feeding approaches.

For the 2-D spatial diversity extension, all four techniques in Fig. 12 have advantages and drawbacks. MIMO extension is the most potent technique, but it suffers from high cost. Diplexer extension features simplicity, but only applies to a simple single-object tracking scenario. Multiplexing extensions have low costs and high performance benefits, but suffer from complicated designs and huge spectrum usage. Power divider extension, combined with a random phase coding technique, offers architectural simplicity while inherently compromising SNR performance to attain enhanced diversity. In the future, a combination of these available techniques or some new novel extension techniques may be explored for various applications.

### 2) ISAC Applications:

As introduced in Sec. III, frequency-diverse imaging and sensing share a similar architecture with MIMO communication systems while also being able to be cast as an analogous linear inverse problem. This connection will not only deepen our understanding of the underlying mechanisms but also inspire more interesting interdisciplinary research for ISAC applications in the future.

First of all, the similarity between MIMO communication and frequency-diverse imaging suggests that some techniques can be transferred between them. For instance, water-filling algorithms in MIMO communication optimize power allocation across multiple channels to maximize total capacity by distributing more power to stronger subchannels and less to weaker ones, analogous to filling a container with water to a uniform level. This may also be applied to frequency-diverse imaging and sensing for power allocation. Additionally, while beamforming is widely used in MIMO, its counterpart in frequency-diverse imaging systems (waveform or spectrum design) remains underexplored.

Additionally, the frequency-dependent nature of frequency-diverse imaging shares similarities with the OFDM scheme in wireless communication, suggesting that frequency-diverse imaging and sensing could be implemented within an OFDM communication system. This concept has been preliminarily investigated in [91], where a high-scanning-rate frequency-diverse antenna was integrated into an OFDM receiver for direction-of-arrival estimation. Additional ISAC applications could be explored using this architecture in the future.

Finally, the deep integration of frequency-diverse sensing and MIMO communication remains largely unexplored, as only recently developed extremely-high-scanning-rate frequency-diverse antennas can satisfy the narrowband requirements of communication systems. Recently, the integration of frequency-diverse sensing and backscatter communication has been investigated in [16], as both can be addressed through inverse scattering approaches. However, ISAC implementations combining frequency-diverse sensing with MIMO communication have not yet been explored, suggesting significant opportunities in these interdisciplinary areas.

In summary, this paper has systematically introduced frequency-diverse imaging and sensing. As a rapidly evolving field, this technology will continue to pioneer innovative approaches, demonstrating remarkable potential to drive paradigm-shifting advancements in future applications.

## REFERENCES

- [1] T. M. Grzegorczyk, P. M. Meaney, P. A. Kaufman, R. M. diFlorio Alexander, and K. D. Paulsen, "Fast 3-D tomographic microwave imaging for breast cancer detection," *IEEE Transactions on Medical Imaging*, vol. 31, no. 8, pp. 1584–1592, 2012.
- [2] F. Yang, L. Sun, Z. Hu, H. Wang, D. Pan, R. Wu, X. Zhang, Y. Chen, and Q. Zhang, "A large-scale clinical trial of radar-based microwave breast imaging for asian women: Phase I," in *2017 IEEE International Symposium on Antennas and Propagation & USNC/URSI National Radio Science Meeting*, 2017, pp. 781–783.
- [3] A. Phager, S. Candefjord, M. Elam, and M. Persson, "Microwave diagnostics ahead: Saving time and the lives of trauma and stroke patients," *IEEE Microwave Magazine*, vol. 19, no. 3, pp. 78–90, 2018.
- [4] M. Hopfer, R. Planas, A. Hamidipour, T. Henriksson, and S. Semenov, "Electromagnetic tomography for detection, differentiation, and monitoring of brain stroke: A virtual data and human head phantom study," *IEEE Antennas and Propagation Magazine*, vol. 59, no. 5, pp. 86–97, 2017.
- [5] F. Fioranelli, J. Le Kernec, and S. A. Shah, "Radar for health care: Recognizing human activities and monitoring vital signs," *IEEE Potentials*, vol. 38, no. 4, pp. 16–23, 2019.
- [6] Y. Li, S. Dong, and C. Gu, "Feel your heartbeat across space: Radar-based cardiac activity monitoring for healthcare applications," *IEEE Microwave Magazine*, vol. 25, no. 12, pp. 91–111, 2024.
- [7] D. Sheen, D. McMakin, and T. Hall, "Three-dimensional millimeter-wave imaging for concealed weapon detection," *IEEE Transactions on Microwave Theory and Techniques*, vol. 49, no. 9, pp. 1581–1592, 2001.
- [8] S. Li and S. Wu, "Low-cost millimeter wave frequency scanning based synthesis aperture imaging system for concealed weapon detection," *IEEE Transactions on Microwave Theory and Techniques*, vol. 70, no. 7, pp. 3688–3699, 2022.
- [9] H. Mei, H. Jiang, J. Chen, F. Yin, L. Wang, and M. Farzaneh, "Detection of internal defects of full-size composite insulators based on microwave technique," *IEEE Transactions on Instrumentation and Measurement*, vol. 70, pp. 1–10, 2021.
- [10] Q. Cuong Bui, W. Lin, Q. Huang, and G.-S. Byun, "Automated internal defect identification and localization based on a near-field SAR millimeter-wave imaging system," *IEEE Access*, vol. 13, pp. 24 698–24 716, 2025.
- [11] D. Schwarz, N. Riese, I. Dorsch, and C. Waldschmidt, "System performance of a 79 GHz high-resolution 4D imaging MIMO radar with 1728 virtual channels," *IEEE Journal of Microwaves*, vol. 2, no. 4, pp. 637–647, 2022.
- [12] C. Waldschmidt, J. Hasch, and W. Menzel, "Automotive radar — from first efforts to future systems," *IEEE Journal of Microwaves*, vol. 1, no. 1, pp. 135–148, 2021.
- [13] Y. Hai, Z. Su, J. Wu, K. C. Teh, Z. Shao, W. Pu, R. Li, Y. Huang, and J. Yang, "Deep spectral sensing and reconstruction for high-resolution imaging of MWP-SAR in complex electromagnetic environments," *IEEE Transactions on Geoscience and Remote Sensing*, vol. 62, pp. 1–15, 2024.
- [14] F. Liu, Y. Cui, C. Masouros, J. Xu, T. X. Han, Y. C. Eldar, and S. Buzzi, "Integrated sensing and communications: Toward dual-functional wireless networks for 6G and beyond," *IEEE Journal on Selected Areas in Communications*, vol. 40, no. 6, pp. 1728–1767, 2022.
- [15] Q. Zhang, B. Liu, S.-W. Wong, K.-F. Tong, K.-K. Wong, and H. Wong, "Guest editorial: Special cluster on smart surfaces, antennas, and propagation for integrated sensing and communication (ISAC)," *IEEE Antennas and Wireless Propagation Letters*, vol. 23, no. 11, pp. 3402–3405, 2024.
- [16] D. Ma, W. Xu, C. Zhang, H. Zhou, S. Shen, Q. Zhang, and Y. Fang, "Frequency-diverse integrated sensing and backscatter communication system utilizing high scanning-rate slot array antenna with inverse scattering approach," *TechRxiv*, Jul. 2025.
- [17] S. Xiao, Z. Chang, J. Du, G. Zhang, A. K. Rashid, Y. Huang, C. Duan, D. Zhang, and Q. Zhang, "Demonstration of multitarget wireless sensing using high-scanning-rate coupled-patch antenna," *IEEE Antennas and Wireless Propagation Letters*, vol. 23, no. 11, pp. 3406–3410, 2024.
- [18] G. Krieger, "MIMO-SAR: Opportunities and pitfalls," *IEEE Transactions on Geoscience and Remote Sensing*, vol. 52, no. 5, pp. 2628–2645, 2014.
- [19] M. E. Yanik and M. Torlak, "Near-field MIMO-SAR millimeter-wave imaging with sparsely sampled aperture data," *IEEE Access*, vol. 7, pp. 31 801–31 819, 2019.
- [20] A. Dürr, D. Schwarz, S. Häfner, M. Geiger, F. Roos, M. Hitzler, P. Hügler, R. Thomä, and C. Waldschmidt, "High-resolution 160-GHz imaging MIMO radar using MMICs with on-chip frequency synthesizers," *IEEE Transactions on Microwave Theory and Techniques*, vol. 67, no. 9, pp. 3897–3907, 2019.
- [21] S. S. Ahmed, "Microwave imaging in security — two decades of innovation," *IEEE Journal of Microwaves*, vol. 1, no. 1, pp. 191–201, 2021.
- [22] D. Tajik, F. Foroutan, D. S. Shumakov, A. D. Pitcher, and N. K. Nikolova, "Real-time microwave imaging of a compressed breast phantom with planar scanning," *IEEE Journal of Electromagnetics, RF and Microwaves in Medicine and Biology*, vol. 2, no. 3, pp. 154–162, 2018.
- [23] M. T. Ghasr, D. Pommerenke, J. T. Case, A. McClanahan, A. Aflaki-Beni, M. Abou-Khousa, S. Kharkovsky, K. Quinn, F. De Paulis, and R. Zoughi, "Rapid rotary scanner and portable coherent wideband Q-band transceiver for high-resolution millimeter-wave imaging applications," *IEEE Transactions on Instrumentation and Measurement*, vol. 60, no. 1, pp. 186–197, 2011.
- [24] T. V. Hoang, V. Fusco, T. Fromenteze, and O. Yurduseven, "Computational polarimetric imaging using two-dimensional dynamic metasurface apertures," *IEEE Open Journal of Antennas and Propagation*, vol. 2, pp. 488–497, 2021.
- [25] A. E. Stancombe, K. S. Bialkowski, and A. M. Abbosh, "Portable microwave head imaging system using software-defined radio and switching network," *IEEE Journal of Electromagnetics, RF and Microwaves in Medicine and Biology*, vol. 3, no. 4, pp. 284–291, 2019.
- [26] S.-X. Huang, G.-B. Wu, J.-Y. Dai, K. Fai Chan, Q. Cheng, T.-J. Cui, and C. Hou Chan, "Enabling real-time near-field focusing imaging with space-time-coding metasurface antenna," *IEEE Transactions on Antennas and Propagation*, vol. 72, no. 12, pp. 9082–9094, 2024.
- [27] X. Gu, A. Valdes-Garcia, A. Natarajan, B. Sadhu, D. Liu, and S. K. Reynolds, "W-band scalable phased arrays for imaging and communications," *IEEE Communications Magazine*, vol. 53, no. 4, pp. 196–204, 2015.
- [28] L. Marzall, M. Robinson, P. Danielson, A. Robinson, N. Ehsan, and Z. Popović, "Active and passive components for broadband transmit phased arrays: Broadband transmit front-end components," *IEEE Microwave Magazine*, vol. 23, no. 2, pp. 56–74, 2022.
- [29] J. Hunt, T. Driscoll, A. Mrozack, G. Lipworth, M. Reynolds, D. Brady, and D. R. Smith, "Metamaterial apertures for computational imaging," *Science*, vol. 339, no. 6117, pp. 310–313, 2013.
- [30] D. L. Marks, O. Yurduseven, and D. R. Smith, "Cavity-backed metasurface antennas and their application to frequency diversity imaging," *J. Opt. Soc. Am. A*, vol. 34, no. 4, pp. 472–480, Apr 2017.

- [31] B. Liu, J. Wu, Q. Zhang, and H. Wong, "High-speed wide-angle sensing and imaging by wideband metasurfaces with joint frequency, polarization, and spatial diversities," *Laser & Photonics Reviews*, vol. 18, no. 9, p. 2400207, 2024.
- [32] X. Chen, Y. Wei, J. Wu, J. DU, D. Ma, B. Liu, and Q. Zhang, "Low-profile broadband 1-bit randomly encoded folded reflectarray co-aperture transceiver for frequency-diverse microwave imaging," *IEEE Antennas and Wireless Propagation Letters*, vol. 23, no. 11, pp. 3426–3430, 2024.
- [33] M. Nie, D. Ma, and Q. Zhang, "Frequency-diverse near-field sensing and hand gesture recognition using multimode resonant antenna and convolutional neural network," *IEEE Antennas and Wireless Propagation Letters*, vol. 23, no. 11, pp. 3411–3415, 2024.
- [34] D. Ma, J. Zhong, S. Shen, A. Dubey, C. Zhang, Q. Zhang, and R. Murch, "Single-shot frequency-diverse near-field imaging using high-scanning-rate leaky-wave antenna," *IEEE Transactions on Microwave Theory and Techniques*, vol. 69, no. 7, pp. 3399–3412, 2021.
- [35] D. Ma, Y. Zhang, A. Dubey, S. Deshmukh, S. Shen, Q. Zhang, and R. Murch, "Millimeter-wave 3-D imaging using leaky-wave antennas and an extended rylov approximation in a frequency-diverse MIMO system," *IEEE Transactions on Microwave Theory and Techniques*, vol. 71, no. 4, pp. 1809–1825, 2023.
- [36] Y. Wei, X. Chen, B. Liu, Y. Huang, C. Duan, and Q. Zhang, "2-D single-port phase coding meta-antenna leveraging frequency diversity for microwave imaging," *IEEE Antennas and Wireless Propagation Letters*, vol. 23, no. 11, pp. 3421–3425, 2024.
- [37] O. Yurduseven, J. N. Gollub, D. L. Marks, and D. R. Smith, "Frequency-diverse microwave imaging using planar Mills-Cross cavity apertures," *Opt. Express*, vol. 24, no. 8, pp. 8907–8925, Apr 2016.
- [38] M. F. Imani, J. N. Gollub, O. Yurduseven, A. V. Diebold, M. Boyarsky, T. Fromenteze, L. Pulido-Mancera, T. Slesman, and D. R. Smith, "Review of metasurface antennas for computational microwave imaging," *IEEE Transactions on Antennas and Propagation*, vol. 68, no. 3, pp. 1860–1875, 2020.
- [39] Y. Feng, Q. Hu, K. Qu, W. Yang, Y. Zheng, and K. Chen, "Reconfigurable intelligent surfaces: Design, implementation, and practical demonstration," *Electromagnetic Science*, vol. 1, no. 2, pp. 1–21, 2023.
- [40] C. Liu, F. Yang, S. Xu, and M. Li, "Reconfigurable metasurface: A systematic categorization and recent advances," *Electromagnetic Science*, vol. 1, no. 4, pp. 1–23, 2023.
- [41] I. Jung, Z. Peng, and Y. Rahmat-Samii, "Recent advances in reconfigurable electromagnetic surfaces: Engineering design, full-wave analysis, and large-scale optimization," *Electromagnetic Science*, vol. 2, no. 3, pp. 1–25, 2024.
- [42] J. Chen and Q. Zhang, "High scanning-rate periodic leaky-wave antennas using complementary microstrip-slotline stubs," in *2017 Sixth Asia-Pacific Conference on Antennas and Propagation (APCAP)*, 2017, pp. 1–3.
- [43] D.-F. Guan, Q. Zhang, P. You, Z.-B. Yang, Y. Zhou, and S.-W. Yong, "Scanning rate enhancement of leaky-wave antennas using slow-wave substrate integrated waveguide structure," *IEEE Transactions on Antennas and Propagation*, vol. 66, no. 7, pp. 3747–3751, 2018.
- [44] G. Zhang, Q. Zhang, S. Ge, Y. Chen, and R. D. Murch, "High scanning-rate leaky-wave antenna using complementary microstrip-slot stubs," *IEEE Transactions on Antennas and Propagation*, vol. 67, no. 5, pp. 2913–2922, 2019.
- [45] G. Zhang, Q. Zhang, Y. Chen, and R. D. Murch, "High-scanning-rate and wide-angle leaky-wave antennas based on glide-symmetry Goubau line," *IEEE Transactions on Antennas and Propagation*, vol. 68, no. 4, pp. 2531–2540, 2020.
- [46] X.-L. Tang, Q. Zhang, S. Hu, Y. Zhuang, A. Kandwal, G. Zhang, and Y. Chen, "Continuous beam steering through broadside using asymmetrically modulated goubau line leaky-wave antennas," *Scientific Reports*, vol. 7, no. 1, p. 11685, 2017.
- [47] Q. Zhang, Q. Zhang, and Y. Chen, "Spoof surface plasmon polariton leaky-wave antennas using periodically loaded patches above PEC and AMC ground planes," *IEEE Antennas and Wireless Propagation Letters*, vol. 16, pp. 3014–3017, 2017.
- [48] K. Rudramuni, K. Kandasamy, Q. Zhang, X.-L. Tang, A. Kandwal, P. K. T. Rajanna, and H. Liu, "Goubau-line leaky-wave antenna for wide-angle beam scanning from backfire to endfire," *IEEE Antennas and Wireless Propagation Letters*, vol. 17, no. 8, pp. 1571–1574, 2018.
- [49] S. Ge, Q. Zhang, A. K. Rashid, Y. Zhang, H. Wang, and R. Murch, "A compact full-space scanning leaky-wave antenna with stable peak gain," *IEEE Transactions on Antennas and Propagation*, vol. 69, no. 10, pp. 6924–6929, 2021.
- [50] H. Jiang, K. Xu, Q. Zhang, Y. Yang, D. K. Karmokar, S. Chen, P. Zhao, G. Wang, and L. Peng, "Backward-to-forward wide-angle fast beam-scanning leaky-wave antenna with consistent gain," *IEEE Transactions on Antennas and Propagation*, vol. 69, no. 5, pp. 2987–2992, 2021.
- [51] J. Zhong, A. K. Rashid, and Q. Zhang, "45° linearly polarized and circularly polarized high-scanning-rate leaky-wave antennas based on slotted substrate integrated waveguide," *IEEE Access*, vol. 8, pp. 82 162–82 172, 2020.
- [52] G. Zhang, Q. Zhang, Y. Chen, T. Guo, C. Caloz, and R. D. Murch, "Dispersive feeding network for arbitrary frequency beam scanning in array antennas," *IEEE Transactions on Antennas and Propagation*, vol. 65, no. 6, pp. 3033–3040, 2017.
- [53] H. Zhou, Y. Zhang, Q. Zhang, M. Yu, H. Wang, and R. D. Murch, "Design of coupled-resonator array antenna for steering beam with extremely high scanning rate," *IEEE Transactions on Antennas and Propagation*, vol. 70, no. 8, pp. 7228–7233, 2022.
- [54] S. Xiao, H. Zhou, A. K. Rashid, Y. Zhang, Y. Zhang, Z. Yuan, Z. Zhang, M. Yu, and Q. Zhang, "Codesign of characteristic mode and coupling matrix for frequency-scanning coupled-patch arrays," *IEEE Transactions on Antennas and Propagation*, vol. 72, no. 8, pp. 6777–6782, 2024.
- [55] W. Xu, H. Zhou, B. Liu, X. Zhang, M. Yu, and Q. Zhang, "Extremely high-scanning-rate slot array antenna employing uniplanar-coupled waveguide cavities," *IEEE Antennas and Wireless Propagation Letters*, vol. 23, no. 12, pp. 4837–4841, 2024.
- [56] W. Xu, D. Ma, P. Jiang, C. Yu, K. Gong, B. Liu, S. Shen, and Q. Zhang, "Frequency-diverse integrated sensing and communication system utilizing coupled-resonator LWA with full-space coverage and high scanning rate," *TechRxiv*, April 2025.
- [57] W. Zhang, L. Li, and F. Li, "Multifrequency imaging from intensity-only data using the phaseless data distorted rylov iterative method," *IEEE Transactions on Antennas and Propagation*, vol. 57, no. 1, pp. 290–295, 2009.
- [58] V. H. Rumsey, "Reaction concept in electromagnetic theory," *Phys. Rev.*, vol. 94, pp. 1483–1491, Jun 1954.
- [59] R. F. Harrington, *Time-harmonic electromagnetic fields*. McGraw-Hill, 1961.
- [60] C. C. Weng, "Waves and fields in inhomogenous media," *Wiley IEEE Press*, 1999.
- [61] Q. Zhang, D. Ma, X. Tang, G. Zhang, Z. Zhang, K. Xu, X. Ye, Y. Sun, and R. D. Murch, "1-D frequency-diverse single-shot guided-wave imaging using surface-wave goubau line," *IEEE Transactions on Antennas and Propagation*, vol. 68, no. 4, pp. 3194–3206, 2020.
- [62] G. H. Golub and C. F. Van Loan, *Matrix Computations*, 4th ed. Baltimore: Johns Hopkins University Press, 2013.
- [63] H. Andrews and C. Patterson, "Singular value decompositions and digital image processing," *IEEE Transactions on Acoustics, Speech, and Signal Processing*, vol. 24, no. 1, pp. 26–53, 1976.
- [64] P. Kanjilal and S. Palit, "On multiple pattern extraction using singular value decomposition," *IEEE Transactions on Signal Processing*, vol. 43, no. 6, pp. 1536–1540, 1995.
- [65] T. J. Willink, "Efficient adaptive svd algorithm for mimo applications," *IEEE Transactions on Signal Processing*, vol. 56, no. 2, pp. 615–622, 2008.
- [66] J. A. Rosenfeld and R. Kamalapurkar, "Dynamic mode decomposition with control liouville operators," *IEEE Transactions on Automatic Control*, vol. 69, no. 12, pp. 8571–8586, 2024.
- [67] G. W. Stewart, "On the early history of the singular value decomposition," *SIAM Review*, vol. 35, no. 4, pp. 551–566, 1993.
- [68] M. Gavish and D. L. Donoho, "The optimal hard threshold for singular values is  $4/\sqrt{3}$ ," *IEEE Transactions on Information Theory*, vol. 60, no. 8, pp. 5040–5053, 2014.
- [69] C. Eckart and G. Young, "The approximation of one matrix by another of lower rank," *Psychometrika*, vol. 1, no. 3, pp. 211–218, 1936.
- [70] J. Du, Q. Zhang, B. Liu, Y. Huang, C. Duan, C. H. Chan, and Q. Zhang, "Probe-free high-resolution millimeter-wave frequency-diverse sensing based on spoof surface plasmon polaritons," *IEEE Transactions on Antennas and Propagation*, vol. 72, no. 1, pp. 1057–1062, 2024.
- [71] Y. Wei, X. Chen, and Q. Zhang, "Two-dimensional spectrum-efficient meta-antenna for probe-free frequency-diverse imaging and hand gesture recognition," *TechRxiv*, Apr. 2025.

- [72] D. Tse and P. Viswanath, *Fundamentals of Wireless Communication*. Cambridge University Press, 2005.
- [73] J. A. Martinez Lorenzo, J. Heredia Juesas, and W. Blackwell, "A single-transceiver compressive reflector antenna for high-sensing-capacity imaging," *IEEE Antennas and Wireless Propagation Letters*, vol. 15, pp. 968–971, 2016.
- [74] D. Zheng and K. Wu, "Multifunctional filtering leaky-wave antenna exhibiting simultaneous rapid beam-scanning and frequency-selective characteristics based on radiative bandpass filter concept," *IEEE Transactions on Antennas and Propagation*, vol. 68, no. 8, pp. 5842–5854, 2020.
- [75] C. Vázquez, C. García, Y. Álvarez, S. Ver-Hoeve, and F. Las-Heras, "Near field characterization of an imaging system based on a frequency scanning antenna array," *IEEE Transactions on Antennas and Propagation*, vol. 61, no. 5, pp. 2874–2879, 2013.
- [76] A. J. Mackay and G. V. Eleftheriades, "Meandered and dispersion-enhanced planar leaky-wave antenna with fast beam scanning," *IEEE Antennas and Wireless Propagation Letters*, vol. 20, no. 8, pp. 1596–1600, 2021.
- [77] S.-D. Xu, D.-F. Guan, Q. Zhang, P. You, S. Ge, X.-X. Hou, Z.-B. Yang, and S.-W. Yong, "A wide-angle narrowband leaky-wave antenna based on substrate integrated waveguide-spoof surface plasmon polariton structure," *IEEE Antennas and Wireless Propagation Letters*, vol. 18, no. 7, pp. 1386–1389, 2019.
- [78] J. Chen, W. Yuan, W. X. Tang, L. Wang, Q. Cheng, and T. J. Cui, "Linearly sweeping leaky-wave antenna with high scanning rate," *IEEE Transactions on Antennas and Propagation*, vol. 69, no. 6, pp. 3214–3223, 2021.
- [79] Z. Peng, W. Yang, S. Shi, M. Jiang, J. Gao, and G. Zhai, "High scanning rate asymmetrical dual-beam leaky wave antenna using sinusoidally modulated reactance superposing surface," *IEEE Transactions on Antennas and Propagation*, vol. 70, no. 12, pp. 12 258–12 263, 2022.
- [80] L. Jidi, X. Cao, J. Gao, T. Li, H. Yang, and S. Li, "Ultrawide-angle and high-scanning-rate leaky wave antenna based on spoof surface plasmon polaritons," *IEEE Transactions on Antennas and Propagation*, vol. 70, no. 3, pp. 2312–2317, 2022.
- [81] Z. Wu, J. Wang, L. Zhao, and Z. Shen, "Full-space and high-scanning-rate leaky-wave antenna based on spoof surface plasmon polaritons," *IEEE Antennas and Wireless Propagation Letters*, vol. 23, no. 2, pp. 693–697, 2024.
- [82] W. Xu, H. Z. Zhou, J. Du, and Q. Zhang, "Full-space scanning leaky-wave antenna with high scanning rate and enhanced efficiency via periodic high-Q resonant network loading," *TechRxiv*, May 2025.
- [83] P. Jiang, W. Xu, and Q. Zhang, "Demonstration of multiple-input multiple-output high-scanning-rate coupled-resonator antennas for 2-D multi-target localization and heart beat rate monitoring," *TechRxiv*, April 2025.
- [84] Z. Xu, D. Ma, J. Du, R. Murch, and Q. Zhang, "A 2-D scanning spoof surface plasmon polariton diplexing leaky-wave antenna for sensing applications," *IEEE Transactions on Plasma Science*, pp. 1–7, 2025.
- [85] X. Chen, W. Xu, D. Ma, Y. Wei, B. Liu, and Q. Zhang, "Multiplexing high-scanning-rate frequency scanning antenna for two-dimensional single-shot frequency-diverse microwave imaging," *TechRxiv*, May 2025.
- [86] J. N. Gollub, O. Yurduseven, K. P. Trofatter, D. Arnitz, M. F. Imani, T. Sleasman, M. Boyarsky, A. Rose, A. Pedross-Engel, H. Odabasi, T. Zvolensky, G. Lipworth, D. Brady, D. L. Marks, M. S. Reynolds, and D. R. Smith, "Large metasurface aperture for millimeter wave computational imaging at the human-scale," *Scientific Reports*, vol. 7, no. 1, p. 42650, 2017.
- [87] O. Yurduseven, J. N. Gollub, A. Rose, D. L. Marks, and D. R. Smith, "Design and simulation of a frequency-diverse aperture for imaging of human-scale targets," *IEEE Access*, vol. 4, pp. 5436–5451, 2016.
- [88] X. Chen, Y. Wei, J. Wu, J. DU, D. Ma, B. Liu, and Q. Zhang, "Low-profile broadband 1-bit randomly encoded folded reflectarray co-aperture transceiver for frequency-diverse microwave imaging," *IEEE Antennas and Wireless Propagation Letters*, vol. 23, no. 11, pp. 3426–3430, 2024.
- [89] T. Sleasman, M. Boyarsky, L. Pulido-Mancera, T. Fromenteze, M. F. Imani, M. S. Reynolds, and D. R. Smith, "Experimental synthetic aperture radar with dynamic metasurfaces," *IEEE Transactions on Antennas and Propagation*, vol. 65, no. 12, pp. 6864–6877, 2017.
- [90] B. Liu, J. Wu, Q. Zhang, and H. Wong, "High-speed wide-angle sensing and imaging by wideband metasurfaces with joint frequency, polarization, and spatial diversities," *Laser & Photonics Reviews*, vol. 18, no. 9, p. 2400207, 2024.
- [91] R. S. Zakariyya, X. Wentau, Y. Zhang, R. Wang, Y. Huang, C. Duan, and Q. Zhang, "Joint DoA and CFO estimation scheme with received beam scanned leaky wave antenna for industrial internet of things (IIoT) systems," *IEEE Internet of Things Journal*, vol. 10, no. 15, pp. 13 686–13 696, 2023.
- [92] J. M. Bioucas-Dias and M. A. T. Figueiredo, "A new twist: Two-step iterative shrinkage/thresholding algorithms for image restoration," *IEEE Transactions on Image Processing*, vol. 16, no. 12, pp. 2992–3004, 2007.